UNIVERSITY OF CALIFORNIA
RIVERSIDE

Transition Metal Dichalcogenide Films Deposited in High Vacuum for Electronic and Catalytic Application

A Dissertation submitted in partial satisfaction
of the requirements for the degree of

Doctor of Philosophy

in

Materials Science and Engineering

by

Kortney L. Almeida

March 2021

Dissertation Committee:
Dr. Ludwig Bartels, Chairperson
Dr. Alexander A. Balandin
Dr. Jianlin Liu

The Dissertation of Kortney L. Almeida is approved:

Committee Chairperson

University of California, Riverside

Acknowledgements

I would like to first thank my PI, Dr. Ludwig Bartels, for allowing me to conduct my undergraduate and graduate research in his lab. I was able to gain much knowledge through his guidance and support during my degree. Next, I would like to thank all of my mentors and coworkers, past and present in the Bartels Lab.

Big thanks to the fam (Mom, Dad, Lyni, Sean, Nana.) Also, many thanks to Dad and Gail for your support. And a final thank you to my fellow colleagues and friends Koichi Yamaguchi, Tammy Huang, Tom Empante, and Hae In Yang for their support here at UCR (and outside.)

ABSTRACT OF THE DISSERTATION

Transition Metal Dichalcogenide Films Deposited in High Vacuum for Electronic and Catalytic Application

by

Kortney L. Almeida

Doctor of Philosophy, Graduate Program in Materials Science and Engineering
University of California, Riverside, March 2021
Dr. Ludwig Bartels, Chairperson

Transition metal dichalcogenides (TMDs) are novel materials that possess a direct band-gap when deposited at a single layer thickness. These 2D materials offer properties that set them apart from conventional bulk silicon such as an improved on-off ratio and the potential for photonic application, with the indirect bandgap of silicon being the limit. If implemented commercially, the former will reduce the power consumption of, e.g., memory devices, significantly, while the latter opens up new pathways for on-chip integration of emitter and detectors for optical communication. Continuing miniaturization of semiconducting devices require the incorporation of materials such as these.

We have developed a method that allows deposition of MoS_2 films across large surface areas in high vacuum and at precise thickness control. The chamber was designed to achieve high vacuum at 10^{-7} torr with the goal of maintaining a clean interface during deposition of the material. MoS_2 single-layer films offer an improved on-off ratio for transistor devices leading to lower power consumption in the off state as compared to silicon. The high vacuum nature of this system eliminates concern for contaminants that may result from being in ambient pressures. This allows for creating a cleaner interface for

better functioning electronics such as diodes. We look to incorporate this material with the III-V semiconductor, gallium nitride, as a way to manipulate the band structure in processes unique to this reactor.

These MoS_2 films can also render gold nanoparticles stable and active for carbon monoxide oxidation and higher alcohol formation even on otherwise inert substrates. Previously, this activity of gold had only been observed on reducible bulk oxides like titania and ceria. This method's ability to coat industrial glass surfaces for this application may reduce costs and allow the transition from current platinum catalysts to much "cheaper" gold ones. This research effort may both help in building more energy-efficient microchips and in creating green fuels by higher alcohol formation from biomass gasification and further strengthens homogenous deposition of MoS_2.

Table of Contents

List of Publications

Almeida, K.; Chagoya, K.L.; Felix, A.; Jiang; Le, D. T.; Rawal, T.B.; Evans, P.E.; Wurch, M.; Yamaguchi, K.; Dowben, P.A.; Bartels, L.; Rahman, T.S.; Blair, R.G., Towards Higher Alcohol Formation using a single-layer MoS_2 activated Au on Silica: Methanol Carbonylation to Acetaldehyde. Just Submitted.

Almeida, K.; Pena, P.; Rawal, T.B.; Coley, W.; Akhavi, A.; Wurch, M.; Yamaguchi, K.; Le, D.; Rahman, T.S.; Bartels, L., A Single-Layer of MoS_2 Activates Gold for Room Temperature CO Oxidation on an Inert Silica Substrate. Journal of Physical Chemistry C **2019**, 123, 11, 6592-6598.

Almeida, K.; Wurch, M.; Geremew, A.; Yamaguchi, K.; Empante, T. A.; Valentin, M. D.; Gomez, M.; Berges, A. J.; Stecklein, G.; Rumyantsev, S.; Martinez, J.; Balandin, A. A.; Bartels, L., High-Vacuum Particulate-Free Deposition of Wafer-Scale Mono-, Bi-, and Trilayer Molybdenum Disulfide with Superior Transport Properties. ACS Applied Materials & Interfaces **2018**, 10 (39), 33457-33463.

List of Figures

Chapter 1: Introduction

Chapter 2: Instrumentation

Chapter 3: Growth and Characterization of TMDs

Chapter 1: Introduction

1.1 Transition Metal Dichalcogenides

The research for two-dimensional materials has surged with the emergence of graphene and its application and viability in modern electronics.[1] Graphene is a semi-metallic 2D material that is composed of a single-layer sheet of carbon in a honeycomb lattice and produces excellent electrical conductivity. Although it has promising properties, this material does not exhibit a band-gap due to its semi-metallic nature thus directing more research into other single-layer materials. Transition metal dichalcogenides (TMDs) are novel materials that possess a direct band-gap when deposited at single-layer thickness.[2] This material is held together by strong in plane covalent bonds and consists of a transition metal sandwiched in between two chalcogen atoms. It also offers appreciable on-off ratio and carrier mobility.

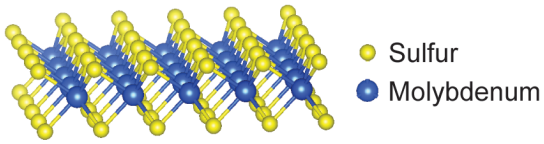

Figure 1.1. Atomic representation of 1L MoS_2.

Molybdenum disulfide is a transition metal dichalcogenide with an indirect band gap at 1.2 eV in the bulk form. It transitions to a direct band gap of 1.9 eV at the single-layer.[3,4] It is natively an n-type semiconducting material although some have proven successful when using a niobium substitutional dopant to make it p-type.[5] It is believed to be natively n-type due to the sulfur deficiencies in the material.[6] Figure 1.1 shows an atomic representation of the single-layer material. MoS_2 has trigonal prismatic structure in the 2H phase.

Methods used to synthesize these materials include mechanical and liquid exfoliation, powder chemical vapor deposition (CVD),[7] metal organic CVD (MOCVD),[8] and atomic layer deposition (ALD).[9] Each of these methods have drawbacks which include powder contamination when using tube furnaces and pyrophoric and costly precursors in MOCVD or ALD processes, etc. Process control over transition metal dichalcogenides is not yet completely realized. Many techniques such as powder and metal organic CVD provide uncontrollable growth varying from single to few layer materials. Also, not all of these methods are capable of wafer scale growth at uniform thickness and great material homogeneity and connectivity. In order to incorporate TMDs into modern electronics and industrially, a conformal growth method is required.

1.2 Gallium Nitride

The introduction of gallium nitride (GaN) revolutionized electronics in many ways. It is a III-IV semiconducting material with a direct band gap at 3.4 eV. High quality GaN was first synthesized using an aluminum nitride (AlN) buffer layer by Amano et. al in 1986.[10] GaN is often grown on three different substrates: silicon carbide (SiC,) sapphire, and silicon. Figure 1.2 shows an atomic representation of the wurtzite structure of Ga-terminated gallium nitride, the more stable structure.[11] There are also instances in which N-terminated GaN is synthesized, although it is the more unstable of the two.[12]

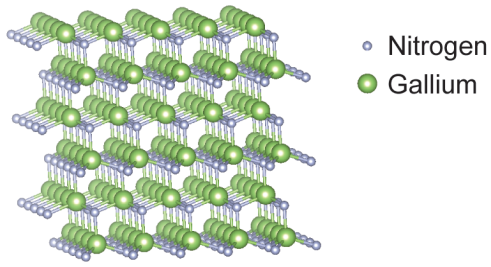

Figure 1.2 Atomic representation of gallium nitride.

One of the early uses of GaN was the ability to create blue light-emitting-diodes from this wide band-gap material doped with Si.[13] Gallium nitride/silicon structures may be used as HFETs in power electronics rather than other materials such as silicon and silicon carbide.[14] It is used due to its breakdown strength and carrier mobility. GaN high electron-mobility transistors (HEMT) are more commercially produced now. Gallium nitride has also been used recently as a material for chargers, as an alternative to silicon. These GaN HEMT chargers are more efficient, smaller, lightweight, and much faster than current silicon-based chargers.[15]

Gallium nitride is naturally an n-type semiconductor due to its nitrogen vacancies while, unlike MoS_2, there is difficulty in obtaining p-type GaN.[16] A magnesium dopant is used for GaN[17] but, oftentimes, it is difficult to activate. Reports state that the substrate must be thermally annealed in order to activate the Mg.[18] This causes issue in the viability and potential for incorporation of p-GaN in heterostructures. As a result, alternative stacked heterostructures must be investigated further. We look to incorporate this material with MoS_2.

Chapter 2: Instrumentation

2.1 High Vacuum Growth Reactor

The system designed for this process is a homebuilt reactor composed of a standard high vacuum stainless steel chamber equipped with a rough pump and turbo pump to achieve 10^{-7} torr; maintaining high vacuum is crucial to this process.

There are two iterations of chambers made for this process. Figure 2.1a shows the first iteration of the chamber that was later improved upon for this work. This particular chamber, schematic shown in figure 2.1b, was equipped with two sets of filaments for the possibility of doped materials and to be able to synthesize two different TMDs: MoS_2 and NbS_2. The homebuilt filament holder contains 0.5 mm Nb and 1.0 mm Mo attached to water-cooled leads so that it does not overheat. The chalcogen source for this chamber is liquid carbon disulfide that is leaked into the chamber via a leak valve (Varian) and a 2-inch heater (MeiVac) is housed in this system as shown in the schematic in figure 2.1b. A standard video camera is on top of the chamber for a view of the hotplate. After much work on the first chamber, another was made to address issues that were involved with the original design.

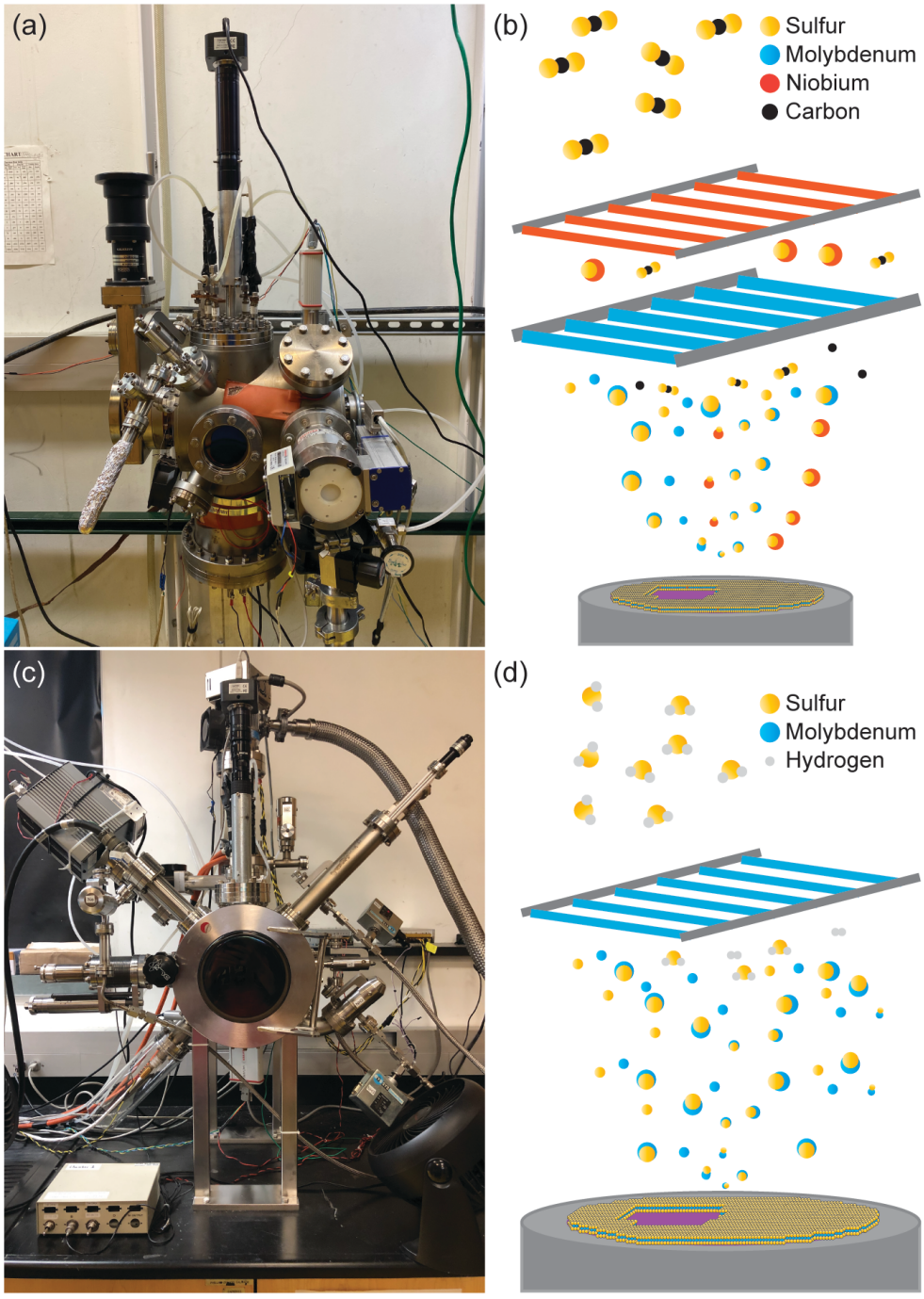

Figure 2.1 (a) First iteration of the chamber worked on with (b) its respective growth process and the two sets of filaments. (c) Second version of the chamber with (d) its respective growth process with different processing gas.

The second chamber, as shown in figure 2.1c, has several ports connected to the main body for further customization. Several process gases (H_2S, H_2, NH_3, Ne, N_2) are attached to this chamber via leak valves. The chalcogen precursor for this system was changed to hydrogen sulfide to account for any contamination that may occur from the use of carbon disulfide. A standard 3-inch heater (MeiVac) is mounted in the center of the chamber for proper heating of the substrate as shown in figure 2.1d. The top of the chamber has a homebuilt filament holder equipped with 0.5 mm transition metal material such as Molybdenum rod (4N, Alfa Aesar) shown in figure 2.1d. A standard video camera (Omax) is attached to the top viewport looking down at the sample. The chamber has a sputter gun attached to a port for in-situ surface treatment of GaN substrates and a Knudsen Cell filled with gallium (3N, Alfa Aesar) for deposition of gallium nitride films. A mass spectrometer is attached for leak testing the various gas lines that are attached to the chamber to ensure a clean processing environment. A z-manipulation rod with a molybdenum shutter is attached to the side of the chamber for controlled testing of the sputter beam.

The filament power supply is controlled remotely for better control over the supplied filament current for reliable production of single and few layer films. The heater is controlled via a power supply (TDK gen lambda 150) remotely controlled. The process is controlled by a LabView program for repeatable and consistent runs.

Important for the implementation of this technique is a hue detection method that is used to control layers of TMD material deposited. The standard camera is utilized for this technique, with a view of the substrate atop the hotplate and works the same way for both

chambers. Process control of the system incorporates the use of a standard video camera that is monitoring the hue of the reflected filament on top of the wafer, as previously mentioned.

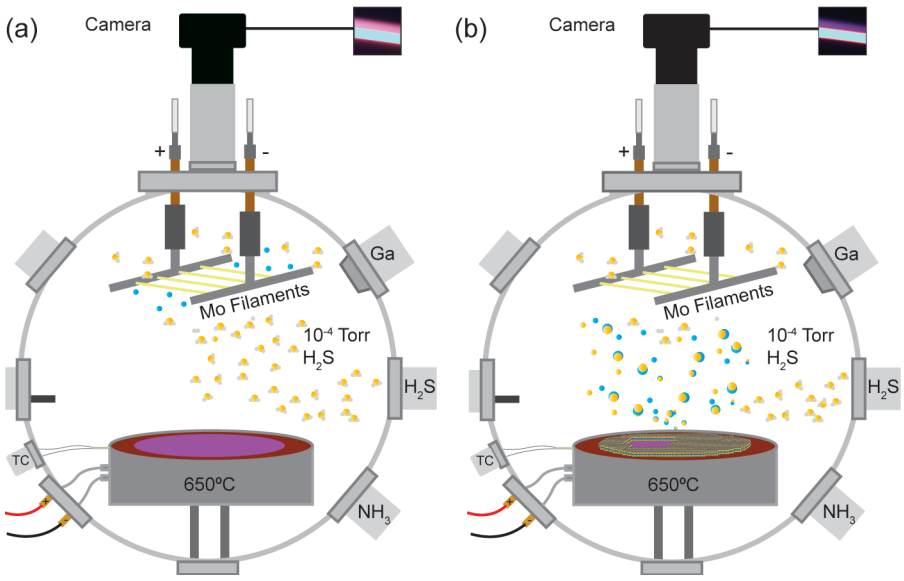

Figure 2.2. (a) Beginning of the growth process showing the precursors being added to the system. (b) Continued growth process, toward the end of the formation of a single layer of film.

In order to grow layered films in this reactor, transition metal filament needs to ramp to white hot in order to get a stable hue reading in the LabView program. Figure 2.2a shows a schematic of the process that occurs for this TMD growth. In this case, hydrogen sulfide gas is shown but other precursors (CS_2) can be used as well. The wafer is first heated to 650ºC and hydrogen sulfide is introduced to 10^{-4} torr. The filaments are then resistively heated by a DC power supply and begin to glow until white hot. At this point, the hue is read via a LabView program that is communicating with the camera. The corresponding initial images are shown in figure 2.2a. The H_2S begins to react at the filament and create MoS_x precursors. As more MoS_x precursors form and the film gets

thicker, the hue gets deeper and transforms into a bluer color than the initial purple hue as shown in figure 2.2b. The filament power can be adjusted according to desired layer thickness, lowered for 2D films or increased for thicker films. This process is described further in the next chapter.

2.2 X-ray Photoelectron Spectroscopy

X-ray photoelectron spectroscopy (XPS) can be used to characterize a few nanometers into a material to determine the elemental composition. A schematic of this process is shown in figure 2.3. The x-ray gun for this work uses an Al k-alpha anode (1486.7 eV.) The x-ray gun is covered by an aluminum foil window as Al has a small z-ratio and is somewhat transparent. The x-ray gun produces x-rays that are directed to the target substrate.

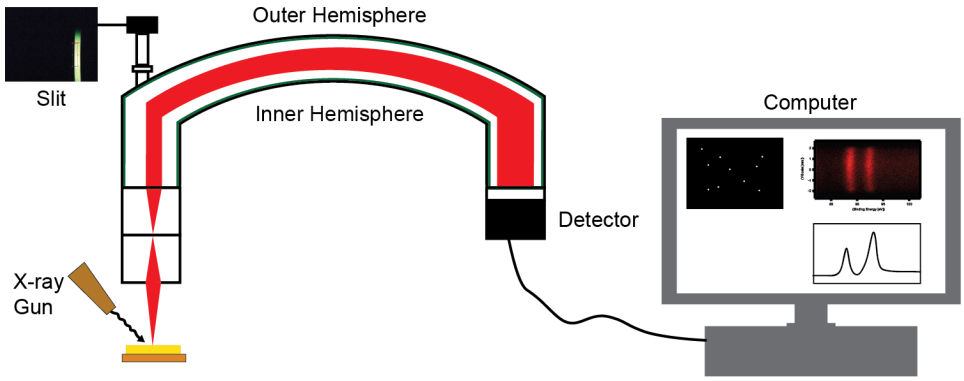

Figure 2.3 Schematic of XPS measurements performed on a gold sample.

Once it hits the substrate, electrons are emitted from the sample and move through the inner and outer hemisphere, at certain voltages (the pass energy,) to be collected at the detector. The pass energy may be lowered for better resolution, but less counts. At the

detector, there are two plates at a certain potential. The electrons are then multiplied and arrive at a phosphor screen to display the secondary electrons from the electron multiplier. The counts hitting the camera correspond to a certain kinetic energy. When converted to binding energy, it produces an image at the screen that corresponds to the y-direction as a function of the binding energy. The subsequent plot is averaged slices of the image shown in the figure. This is equivalent to certain core levels, depending on the elemental composition. This results in information unique to the different materials that are being measured, important for composition of the thin films produced for this work.

2.3 Low Energy Electron Diffraction

Low energy electron diffraction (LEED) is a technique in which a crystalline substrate is hit with an electron beam resulting in the crystals respective diffraction pattern being observed, as shown in Figure 2.4a.

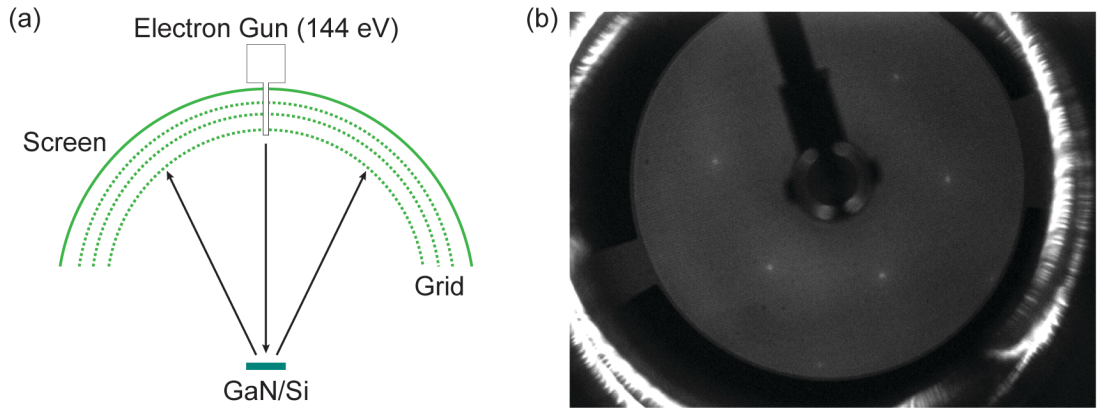

Figure 2.4. (a) Schematic of the electron gun shooting at the surface of a gallium nitride sample and (b) the resultant image at 144 eV.

This characterization technique is primarily used for the study at the gallium nitride surface. Figure 2.4b shows an example diffraction pattern of a gallium nitride substrate

with the resultant pattern indicating the hexagonal symmetry of crystalline GaN. This technique may probe deeper into the substrate depending on the beam energy of the gun. We look at a range of 50 eV to 300 eV for an understanding of our thin layer materials at the surface and to probe deeper into the heterostructure. This information is based upon the universal curve.

2.4 Ion Sputtering

Ion sputtering is a technique that is used for the cleaning of surfaces prior to analysis techniques such as scanning tunneling microscopy (STM) and XPS. An inert gas (e.g. Ne, Ar, Xe, Kr) is leaked into the system via a leak valve. The ion bombardment source is a dual-filament assembly and is equipped with two tungsten filaments routed to a common.

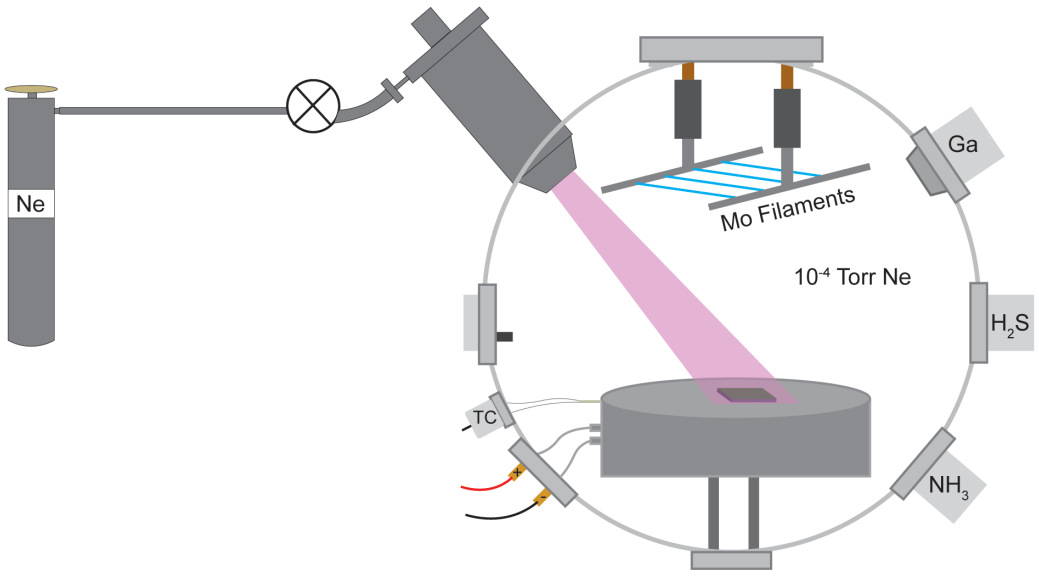

Figure 2.5. Ion sputtering in the high vacuum growth reactor on a blank substrate.

The filament is heated up and the electrons that are emitted are attracted to a positive potential applied to the cage. The electrons impact the inert gas molecules and create ions that are then sent through a set of lenses to accelerate and create a focused ion beam to hit the sample. It operates on the order of 0 to 3000 meV and is equipped with x- and y-deflectors to properly align the beam. The ion source used for this work is for a sputter cleaning treatment of a substrate. A schematic is shown in Figure 2.5 of the sputter process in the high vacuum growth reactor. This technique is also used to sputter away material before e-beam deposition of electrode materials in device fabrication, for clean contacts.

2.5 Device Fabrication

In order to measure the device electrically, device test structures must be fabricated. Typical fabrication techniques for semiconducting devices include electron beam lithography (EBL) and photolithography. For the entirety of this work, devices are fabricated via EBL.

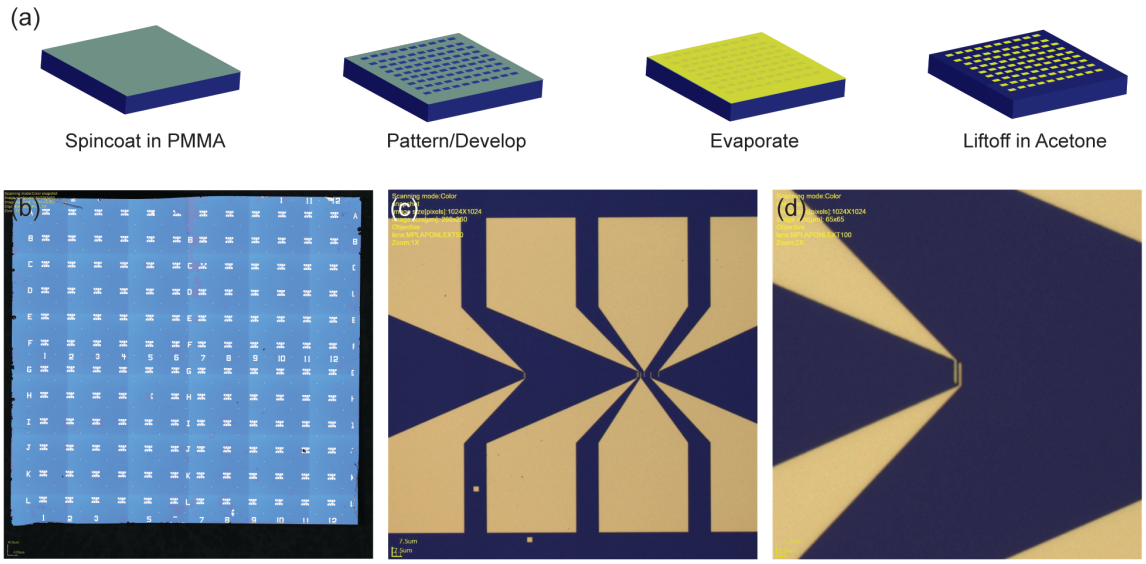

Figure 2.6. (a) Process for the batch fabricated devices on single-layer MoS_2. (b) A fully processed chip and an image of a device at the (c) 50x and the (d) 100x objective.

EBL is used for finer resolutions to define small channels and nanoscale device structures. The substrate is first spun coat with 600 nm of C5 PMMA. The pattern is then created in a crossbeam system that uses an electron beam or via an electron beam lithography system. The PMMA is sensitive to the electron beam as a positive resist and MIBK is used to develop the pattern after it is processed. It is then loaded into an evaporator to deposit the electrode materials. For MoS_2 devices in this work, 5 nm yttrium is used as the adhesion metal and 50 nm of gold as the contact metal. Titanium as an adhesion metal is also used. We look to incorporate an adhesion metal that has a lower

work function for lowered contact resistance[19] The metal is then lifted off in acetone and measured electrically. This process (EBL) can be seen in Figure 2.6(a). The final processed chip is shown in figure 2.6(b-d).

Chapter 3: Growth and Characterization of TMDs

3.1 Molybdenum Disulfide

The following chapter contains excerpts from "High-Vacuum Particulate-Free Deposition of Wafer-Scale Mono-, Bi- and Trilayer Molybdenum Disulfide with Superior Transport Properties" by K. Almeida et. al.

Our process departs significantly from prior work by the use of a set of metallic molybdenum filament wires (Alfa Aesar) as the molybdenum source. Fig. 1a shows a schematic of our growth setup. The method utilizes the difference in volatility between molybdenum metal (melting point: 2623 ºC) and MoS_2 (melting point: 1,185 ºC) as well as other MoS_x species; this ensures that exclusively MoS_x species are released from the filaments. Consequently, the material deposited onto the substrate is already of the correct elemental composition and sufficient surface-mobile to arrange itself into large grains and, ultimately, a continuous film. A background of carbon disulfide gas at a pressure of 6×10^{-4} Torr (compared to a base pressure of the reactor of 1×10^{-7} Torr) is used as a sulfur source for formation of MoS_x species on the filaments and to assure stoichiometry in the resultant film. At a process time of up to 60 min depending on layer number, a continuous and homogeneous single-layer film of MoS_2 is deposited at wafer scale (Fig. 3.1b).

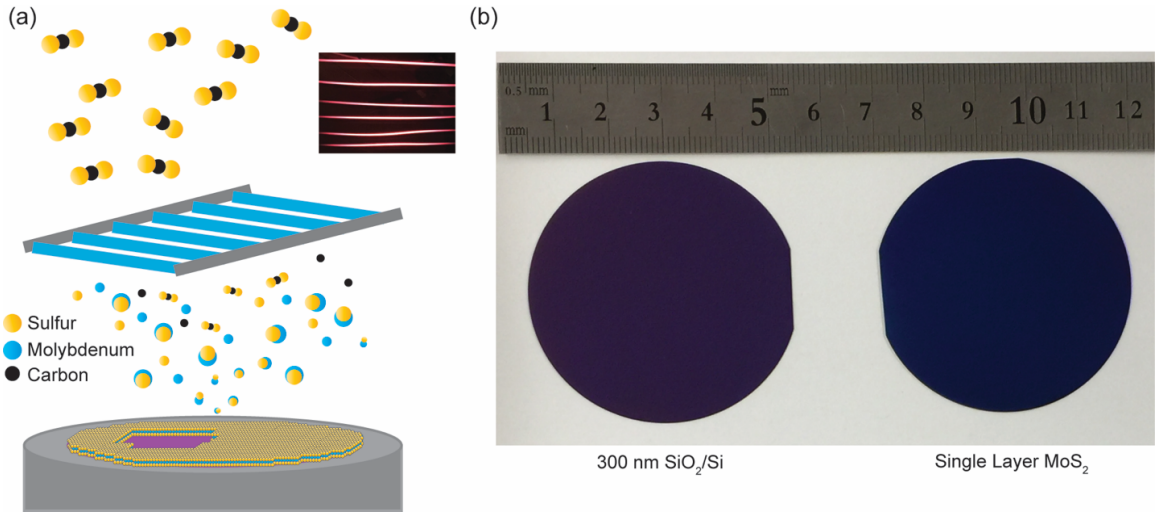

Figure 3.1 (a) Schematic of the high vacuum growth process utilizing a set of directly-heated molybdenum filaments and carbon disulfide as chalcogen source. Volatile MoSx precursors are formed at the filament and precipitate onto the heated substrate coalescing into a continuous and crystalline film. Inset: photograph of heated filaments; (b) photograph of substrates before and after single-layer MoS2 growth.

A number of prior studies[20–22] have addressed the CVD growth of MoS_2 single layers and found a sequence of nucleation and in-plane aggregation. Fig. 3.2a illustrates how we control the film growth: light from the hot molybdenum filaments (inset in Fig. 3.1a) is reflected from the wafer substrate during growth. As CS_2 molecules decompose at the molybdenum filaments, MoS_x precursors evolve, evaporate from the rods, and deposit onto the substrate where they obtain stoichiometric sulfur contents from the environmental CS_2 and form into extended islands - or evaporate again, given the high platen temperature of 650 °C. In a balance between incoming MoS_x species and evaporation of material, the film ripens into larger and larger crystalline islands. The growth rate is highest when a sizable number of large grains have formed that are stable from evaporation and offer edge sites for growth; it is lowest whenever a layer is complete.

In this work we employ concomitant measurement of the hue of the specular-reflected Mo-filament light from the substrate for process control. This approach is novel for process control, but the dependence of the substrate color on single- and few-layer films has been well understood. Blake and Hill described the contrast and color-dependence of graphene on different thickness SiO_2 layers on Si using a multiple internal reflection method.[23] This description has since been expanded, for instance by Zhang et al.,[24] to reveal wavelength/color dependent amplification in MoS2 imaging and spectroscopy.

Figure 3.2 shows the hue value of the light from the molybdenum filament reflected on the substrate as the film is growing layer-by-layer. The hue value is obtained by pointing a video camera from above and through the gaps of the glowing molybdenum rods at the sample during growth. Translation of the camera's red-green-blue (RGB) encoded signal into the common hue-saturation-brightness (HSB) format yields the hue value which cycles through the color circle from 0 to 255. The inset in Figure 3.2 shows the camera view on the filament in the bottom and its reflection from the substrate in the top. Numeric color temperature correction based on the albedo of the filament (bottom) has the power of removing dependence of the hue signal of the reflection (top) from the filament temperature but is not commonly required for growth.

The main graph of Fig. 3.2 shows the evolution of the hue value during growth. Initially the growth is slow due to the absence of growth nuclei and rapid re-evaporation of the material into vacuum. As the growth proceeds, more stable island perimeter becomes available and it speeds up, just to get slower again, when the first layer is about to

complete and the available island perimeter to attach to becomes smaller. This is visible as the first inflection on the hue curve. A growth stopped at this point shows single layer Raman signal, as shown in the inset on the right.

If the growth process is continued at unchanged filament temperature, substrate temperature and CS_2 gas concentration, then a second layer nucleates, increases in size, speeds up in growth, and the growth decelerates again once it nears completion. Stopping the growth at this point, a bilayer film is produced with the corresponding Raman signal (inset). If the film growth is continued, the trilayer color (inset) is reached and ultimately a thick film emerges.

In order to achieve the highest quality films, the actual growth process proceeds not at constant filament brightness as used in the experiment of Fig. 3.2. Rather as each layer nears completion, the filament temperature is reduced gradually to slow down growth and allow optimal ripening/arrangement of the inter-island/domain boundaries as well as evaporation of any adlayer islands that may have formed during the growth process. If another layer is desired, the filament temperature is increased again to speed up film growth and reduced again toward the completion of the next layer.

The Raman spectra in the inset of Fig. 3.2 show the E^1_{2g} in-plane and A_{1g} out-of-plane peaks for different layer thicknesses. The peak separations are 19 (1L), 22 (2L), 23 (3L), and 25 (bulk) cm^{-1}. The separations match well the literature values for mono-, bi-, trilayer and bulk MoS_2 respectively.[3,4]

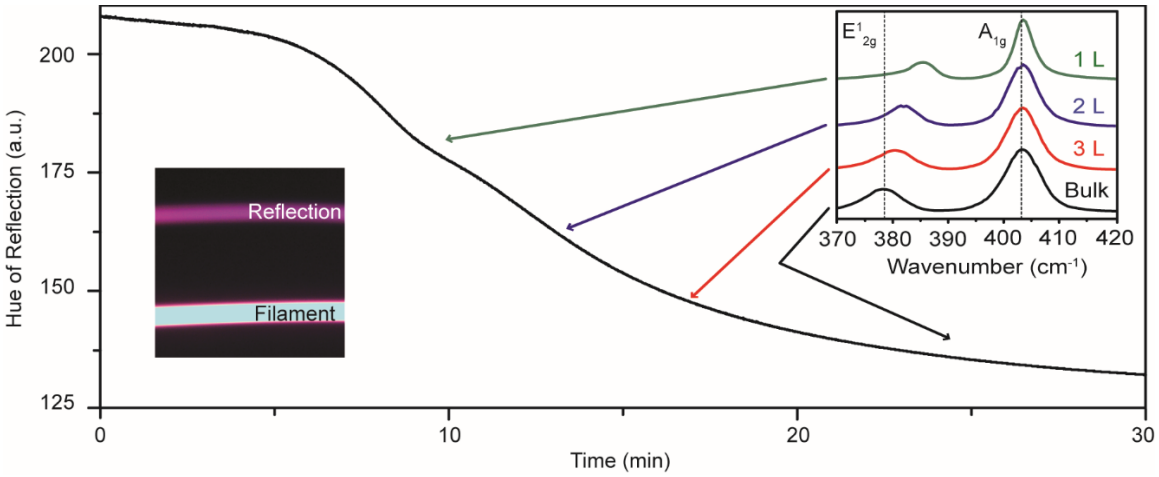

Figure 3.2. Hue of the Mo-rod reflection (top in left inset) during film deposition. The hue-curve reveals the completion of layers, for which Raman spectra are shown in the right inset.

Mapping of the Raman E^1_{2g} and A_{1g} peak separation confirms the homogeneity of the material. Fig. 3.3a-c show millimeter-scale maps of the peak separation; at each layer thickness the variation is well below one wavenumber. The isolated white and black dots are caused by dust deposited onto the sample during Raman mapping in ambient unfiltered air and are not a consequence of the growth process. In order to ascertain the homogeneity of the film over a large range, we took Raman spectra at 840 micron separation across a wafer refocusing the beam at each location. Fig. 3.3d shows the results and affirm the large range homogeneity of the wafer beyond the millimeter-scale map areas of Fig. 3.3a-c.

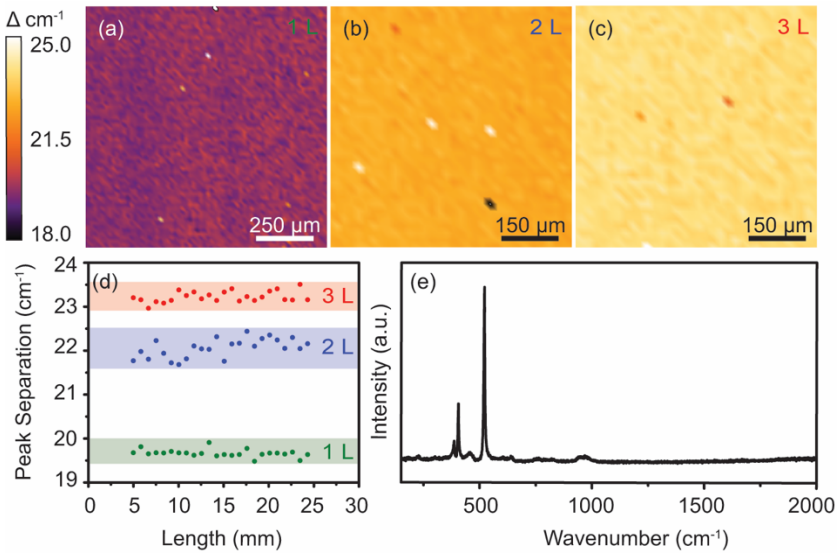

Figure 3.3. (a-c) Spatial mapping of the separation of the in-plane (E^1_{2g}) and out-of-plane (A1g) modes of single-, bi-, and trilayer films, respectively. The values of 19.5, 22, and 23 cm^{-1} are tell-tale of the respective film thickness. (d) Trace of the Raman peak separation in steps of 840 μm steps across one inch of a wafer substrate. (e) Extended range of the Raman spectrum for single layer MoS_2 film.

Despite the use of carbon disulfide as a precursor, we find no Raman signature of a carbon film (Fig. 3.3e). The presence of strong photoluminescence (as strong as on exfoliated samples) is a further indicator of the absence of a carbon film. XPS measurements of the substrate before and after transfer of an MoS_2 film show no significant difference of carbon trace contamination.

The photoluminescence (PL) is an indicator of the film quality and sensitive to adsorbed contaminants, strain and other extrinsic effects. A typical PL spectrum of the film is shown in Fig. 3.4a. The A exciton is found at 1.89-1.90 eV, slightly blue shifted compared to conventional CVD and exfoliated material.[25] We attribute this to strain induced by the higher thermal expansion coefficient of the SiO_2 substrate as compared to the MoS_2 film leading to compressive strain during cool down from growth temperatures,

as is to be expected for a continuous film. Compressive strain of MoS_2 is typically associated with a blue-shift of the PL signature, as observed here.[26] The full width at half maximum of the PL peak is consistently at an excellent value of ~0.077 eV. The PL brightness of the films rivals the best exfoliated and CVD samples we have produced. The B exciton is barely visible at 2.06 eV further confirming the material quality. Mapping of the PL peak position across the sample shows variations on the single-digit millielectronvolt scale only (Fig. 3.4b).

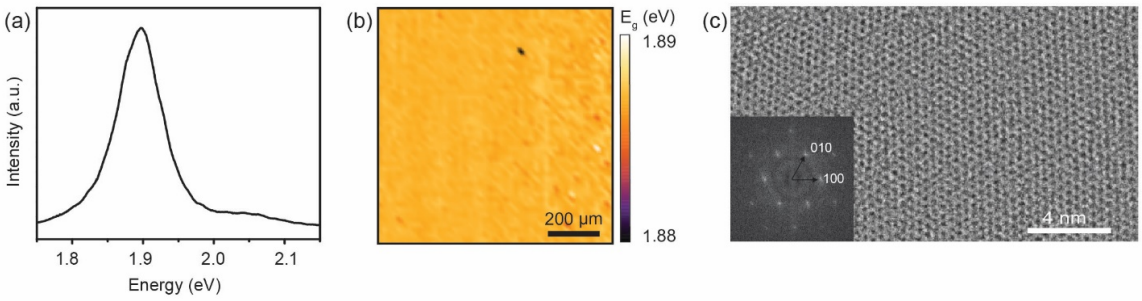

Figure 3.4. (a) Photoluminescence spectrum of a single-layer MoS_2 film. (b) Mapping of the A-exciton position across 1x1 millimeter of sample area reveals variations well below 10 meV (full color scale). (c) STEM image of the crystalline structure of the film. The inset shows the Fourier transformation and two indexed peaks.

Scanning electron microscope images of the MoS_2 single layer film are featureless at any length scale. The AFM root mean square surface roughness is at 0.2 Å slightly better than that of the bare SiO_2 substrate before the growth. Transfer of the film onto a grid for scanning transmission electron microscopy reveals a highly ordered array of MoS_2 unit cells at the expected periodicity (3.31 Å) of the 2H phase (Fig. 3.4c). Extended areas of single-crystalline domains are surrounded by a band of a number of very small (~10 nm) domains, validating the growth mode described above.

Appealing transport properties of the film are crucial for the technological application of the method. Electron beam lithography was used to fabricate 50 field-effect transistor (FETs) test structures using the oxide of the growth substrate as the gate dielectric (bottom-gated without transfer). It is important to highlight that our growth process is sufficiently benign to the substrate that oxide pinholes resulting in gate leakage are absent. We use a device geometry that includes channel length/width of 0.25/20 microns (see insets in Fig. 3.5a for the optical image of the device). The electrodes were fabricated from a stack of 5 nm of yttrium for adhesion and 50 nm of gold. At source-drain voltage V_{sd} below 0.5 V, the output current voltage characteristics (source-drain current I_{sd} as a function of the source-drain voltage V_{sd}) were linear and symmetric indicating near-Ohmic properties of the drain and source contacts. Fig. 5a shows the measured output characteristics at high drain voltage up to 4 V. This biasing condition corresponds to the 160 kV/cm electric field in the channel and power density dissipated by the channel of the order of 109 W/cm^3. The reliable operation of mass-fabricated devices at these extreme conditions indicates the high quality of the material. It is known that the temperature dependence of the current voltage characteristics in this type of MoS_2 transistors is governed by two competing mechanisms: decrease of the threshold voltage and decrease of the mobility with the temperature increase.[27] The superlinearity of the characteristics in Fig. 3.4a can be naturally explained by the Joule heating causing a decrease of the threshold voltage and a small degradation of the mobility.

Fig. 3.5b shows the measured current as a function of applied gate voltage at fixed source-drain biases. The characteristics in Fig. 3.5b do not show any trend of saturation at

high gate voltage and are quite typical for bottom-gated MoS_2 devices in the absence of engineered contacts, such as edge contacts or the use of graphene as a contact material. The low apparent mobility in these devices on the order of 1 can directly be attributed to the common challenge of contacts to MoS_2 devices rather than indicating a property of the film; we expect that integration of top-/dual-gating and engineered contacts would show the full potential of this material.[28–35]

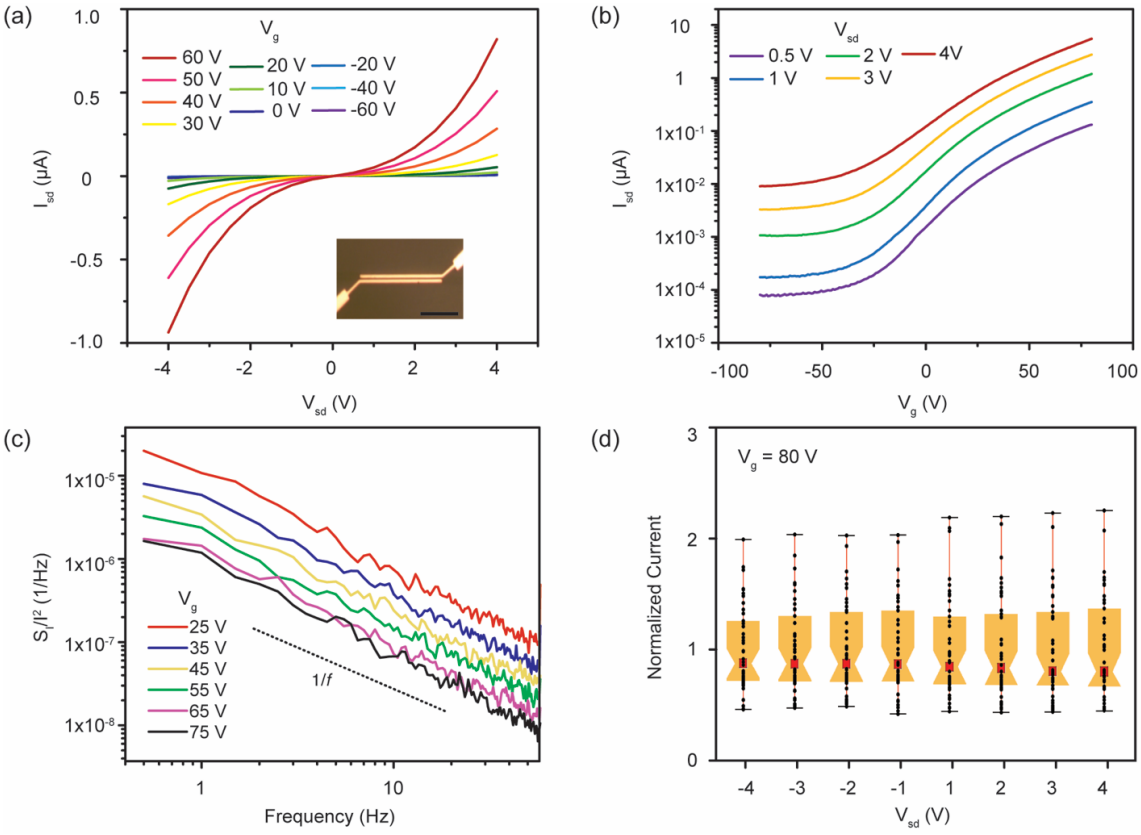

Figure 3.5. (a) IV characteristics of the single layer MoS_2 film at different gate voltages. Inset of an optical image of the device structure. The scale bar is 10 μm. (b) Source-drain current as a function of gate voltage for a single layer MoS_2 device. (c) Noise power as a function of frequency. (d) Box and Whisker plots of the variation of I_{sd} at fixed V_g and for a set of V_{sd}, normalized to the average I_{sd} at the respected V_{sd}. Data is collected from 47 devices evenly spread across >1 cm^2 of substrate area.

The level of the low frequency noise is an important metric of the material quality and suitability for electronic applications.[36] It is particularly important for two-dimensional materials where conduction electrons in the device channel are ultimately exposed to various defects in the gate dielectric and top surface.[37] The level of the low frequency noise can be used to assess the concentration of defects and material tolerance to electromigration. In practical applications, the low frequency noise defines the phase noise in communication systems and sets the limits for sensor sensitivity and selectivity. The low-frequency noise was measured in the frequency range from 1 Hz to 50 Hz at room temperature. The devices were biased in a common source mode. Details of our noise measurement procedures have been reported by some of us elsewhere.[38–40] Fig. 3.5c shows the normalized noise spectral density S_I/I_{ds}^2 as a function of frequency for a representative MoS_2 device. The noise is of clear $1/f$ type (f is a frequency). The absence of the generation – recombination bulges indicates that there are no high concentrations of any specific defect, which would dominate the low frequency noise response. The noise spectral density reveals scaling with the applied gate bias, i.e. carrier concentration in the channel, expected for semiconductor devices.[41] The $1/f$ noise level in field effect transistors is often characterized by the noise amplitude normalized to the channel area.[42] The minimum noise level measured in studied devices was of the order 2×10^{-7} $Hz^{-1}\mu m^2$. This is smaller than that reported in earlier publications for MoS_2 transistors implemented with the exfoliated or CVD material.[39,43] The latter provides an additional confirmation of the material quality from the device applications' point of view.

In order to demonstrate the homogeneity of the film, we fabricated a set 50 devices evenly spaced across more than 1 cm^2 of substrate area. Of the 50 devices fabricated, one had a failure of the electron beam during writing, and two were lithographically nonviable. Fig. 3.5d shows a box and whisker plot of the variation of I_{sd} at different V_{sd} across all remaining 47 devices. We find a maximum variation by a factor of 2 and an interquartile range of 0.8-1.3 with 1 normalized to the average current at any V_{sd}.

In conclusion, the scalable growth of continuous single- and few-layer MoS_2 is demonstrated using a high-vacuum deposition process. Optical and electrical characterizations validate high quality and homogeneity of the material as well as superior noise performance. We highlight that these results are achieved using an amorphous SiO_2 substrate and without any powder or metal−organic precursors. Using the color of light reflected from the substrate, process control at the single-layer limit is achieved.

3.2 Niobium Disulfide

Niobium Disulfide (NbS_2) is another TMD that can be grown using this method. NbS_2 exists in the rhombohedral configuration (3R phase) and in the hexagonal configuration (2H phase) where it has shown to be metallic.[44] This may have application in a variety of electronics.[44–46] The few-layer film was grown using a set of niobium filaments and 10^{-4} torr CS_2 gas at 650°C substrate temperature. The growth proceeds in the same fashion as the MoS_2 including similar filament power used. Figure 3.6a shows the Raman signal obtained from the sample, corresponding to literature sources.[47]

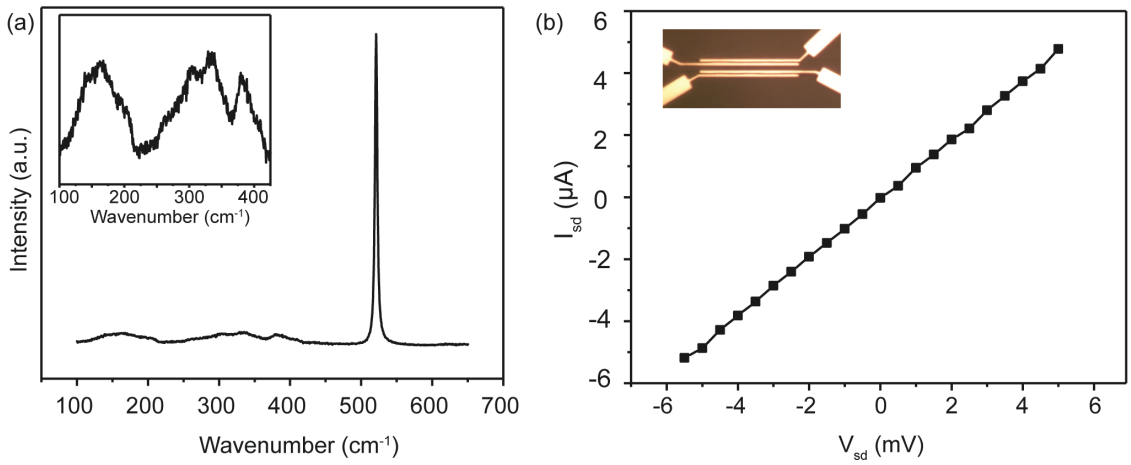

Figure 3.6. (a) Raman spectrum of NbS_2 film. Inset of a zoomed in portion of the spectrum. (b) Electrical transport of NbS_2 250 nm channel. Inset of an image of the device.

A device was also fabricated atop the film. The inset in Figure 3.6b shows an image of the device structure. The device was patterned via EBL and subsequently had 5 nm Yttrium and 50 nm Au deposited and lifted off. Standard IV measurements were performed on the device. The 250 nm channel had produced around 6 μA when 6 mA was applied to the source drain. The transport indicated conducting transport measurements, also indicative of 3R-NbS_2.

The high vacuum growth reactor has shown to grow TMDs beyond MoS_2, extending the possibility to a wide variety of materials that may be used as the transition metal filament (e.g., Mo, Nb, W) or the chalcogen precursor (e.g., CS_2, H_2S, H_2Se.)

Chapter 4: Au-MoS_2 as a Catalyst

4.1 Motivation

The following chapter contains excerpts from "A Single-Layer MoS_2 Activates Au for Room Temperature CO Oxidation on an Inert Silica Substrate" by K. Almeida et. al.

These MoS_2 films can render gold nanoparticles stable and active for carbon monoxide oxidation (like in a car catalyst) and higher alcohol formation even on otherwise inert substrates (glass). Previously, this activity of gold had only been observed on reducible bulk oxides like titania and ceria and this method's ability to coat industrial glass surfaces for this application may reduce costs and allow the transition from current platinum catalysts to much "cheaper" gold ones.

The seminal finding by Haruta of CO oxidation by supported nanoscale gold particles[48] showed that gold, despite being arguably the most noble of metals,[49] can play an active role in heterogeneous catalysis. For the past two decades, the original findings, regarding Au nanoparticles on a titania (TiO_2) support, has been expanded to other oxides,[50–54] in particular, reduceable oxides such as ceria.[55,56] Gold on irreducible, inert substrates continued to prove itself as inert and as catalytically inactive as its bulk form. In the course of the recent broad focus on two-dimensional (2D) materials for catalysis, first indications have emerged that a single-layer of MoS_2 offers a platform for stabilizing nanoscale gold particles and facilitate the requisite electronic states for CO adsorption at room temperature,[57] which is not the case for Au nanoparticles on graphene.[58] Prior theoretical work indicates that gold nanoclusters supported by MoS_2 may be able to support CO oxidation to carbon dioxide,[57,59] differing significantly from Au nanoparticles on graphene.[60,61]

4.2 Carbon Monoxide Oxidation

Here, we report the experimental realization of room temperature CO oxidation on gold nanoparticles on silica covered by a single layer MoS_2 film; we use X-ray photoelectron spectroscopy to monitor repeated CO adsorption and oxidation and offer density functional theory modeling of the reaction pathways.

A large number of catalytic applications of MoS_2 have been proposed both in the past and more recently. Modified MoS_2 is the key catalyst material for industrial hydrodesulfurization; notably, the industrial catalyst material resembles a few-layer film.[62] MoS_2 has also been proposed for alcohol formation[63] and other chemical processes that involve the formation of carbon-oxygen bonds.[64,65] More recently, MoS_2 has gained prominence as a catalyst for hydrogen evolution.[65,66] Its activity has been attributed to edge sites based on low-temperature measurements,[67] and related materials that feature large number of exposed edge sites have been prepared and validated in some catalytic applications.[68–70] Defects on the 2H basal plane can affect the electronic states near the Fermi level depending on the defect geometry and may also forward surface reactions.[71–74]

At issue is whether there are 2D materials that support dispersed Au nanoparticles,[75–77] activate the metal nanoparticles *vis-a-vis* catalysis and suppress sintering of the metallic nanoparticles. Prior computational and experimental results on other two-dimensional materials suggest this concept.[58,78–80] Here we validated the efficacy of this approach for CO oxidation on Au nanoparticles on single-layer MoS_2 on SiO_2 at room temperature.

This manuscript reports on an effort that combines (a) preparation of the centimeter-scale homogeneous MoS_2 film on SiO2 required for (b) lab-based X- ray photoelectron spectroscopy validation of CO oxidative titration with oxygen at room temperature and (c) density functional theory (DFT) modeling that provides atomistic understanding of the CO binding location and catalytic CO oxidation pathway. Figure 4.1 describes the approach schematically.

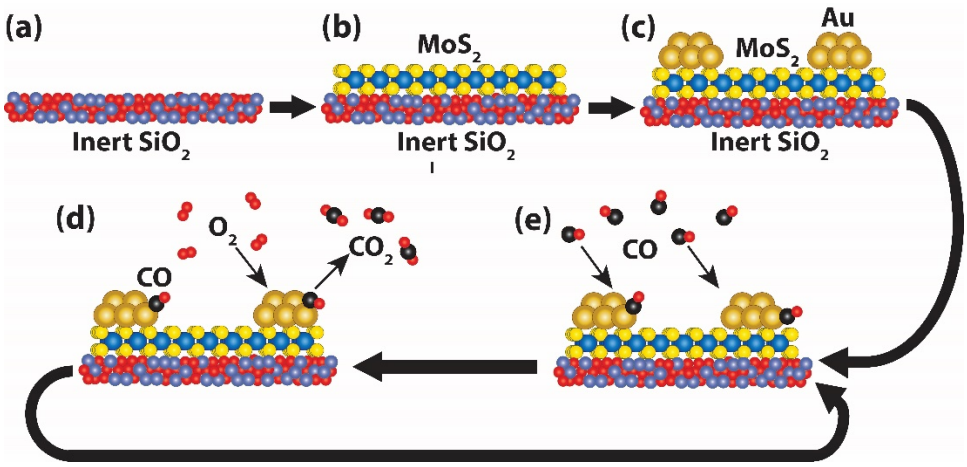

Figure 4.1 Schematic representation of the experimental approach: a) inert SiO_2 substrate is b) coated with a single-layer film of MoS_2 that c) disperses gold deposited onto the film into nanoclusters. d,e) Repeated exposure to first CO and then O_2 leads to cycles of CO adsorption and oxidation without heating the sample above room temperature.

Experimental Results

Sample Preparation: We have developed a technique for coating of inert oxides by an MoS_2 film of controlled integer layer number. Our initial report focused on MoS_2 films on a dry oxide SiO_2 layer on a silicon wafer substrate for electronic applications.[81] This technique is based on heating molybdenum filaments to white glow in high vacuum followed by exposure to carbon disulfide. Decomposition of the disulfide on the filament

surface results in volatile MoS_x precursors, which are precipitated on an inert substrate held at a temperature that affords an equilibrium of MoS_2 island growth and desorption. The growth is monitored via the hue of the reflection of the filament and terminated when it reaches a value of 190 out of 255. Here we report the application of this technique to catalysis using thin (30 nm) silica layers, prepared by plasma-enhanced chemical vapor deposition, as substrate. A thin oxide is used so that electron-based characterization techniques (X-ray photoelectrons spectroscopy, XPS, and scanning electron microscopy, SEM) are applicable. We note, however, that chemically a 30 nm oxide is inert and would not support the reaction or gold activation as described here. Gold deposition used an e-beam evaporator and a quartz crystal microbalance; deposition proceeded at a rate of a fraction of an Angstrom per minute.

Figure 4.2 (a) Raman and (b) photoluminescence spectrum of a single-layer MoS_2 sample before (black) and after (red) 3 Å of gold deposition. Enhancement of the Raman signal by the gold plasmons and quenching of the photoluminescence is observed. (c) SEM image of Au dispersion across the top of a single layer MoS_2 film. A homogeneous distribution of gold clusters each smaller than a few nanometers is observed.

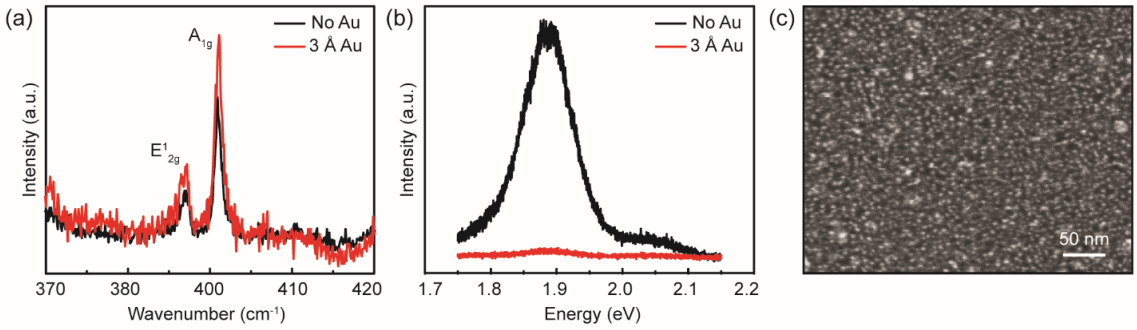

Figure 4.2 shows the characterization of our samples. Before gold deposition we find the typical Raman peak positions for single-layer MoS_2 films for E_{2g} and A_{1g} at 385.5 cm^{-1} and 404.5 cm^{-1} (separation 19 cm^{-1}).[82] After gold deposition, the amplitude of these peaks

is enhanced attesting to the presence of a gold plasmon on the surface that leads to field enhancement.[83] This is typically associated with very small gold nanoparticles, as desired in this study.[75–77] Before gold deposition, the photoluminescence of the substrate material was bright and centered at 1.886 eV with a full-width at half-maximum of 0.0925 eV, the well-established optical bandgap of single-layer MoS_2.[3,4] After gold deposition, the photoluminescence is quenched. This indicates that despite the small gold dosage there is a quenching center within the size of practically any exciton created on the surface. This is further indication for excellent dispersion of gold on MoS_2/SiO_2, much in contrast to gold on bare silica or graphene.

Direct scanning electron microscopy (SEM) image of the sample shows tiny, point-like gold particles below the limit of the instrument for resolution of internal features. These particles are a few nanometers in size at maximum, i.e. in the crucial size range for catalytic activity.[75–77]

CO Oxidation: We use X-ray photoelectron spectroscopy (XPS) to monitor the adsorption and oxidation of carbon dioxide on our sample. XPS experiments utilize a magnesium K(alpha) anode and a hemispherical electron energy analyzer. CO and oxygen gas are dosed into the chamber through a leak valve and pumped out before each measurement cycle.

Computational Details: We perform density functional theory (DFT) calculations as implemented in the Vienna *ab initio* Simulation Package (VASP),[84] employing the projector-augmented wave (PAW).[85,86] As shown in our previous work,[59] the role of van

der Waals (vdW) interaction is important for describing the Au/MoS_2 system. Among the variety of vdW functionals, optB88-vdW[87,88] has been shown to be quite reliable.[89] In this work we thus used the optB88- vdW functional[87,88] to describe electron exchange-correlations. We set the electron kinetic energy cut-off for plane-wave expansion to 500 eV. Similar to our previous work,[59] the simulation supercell consists of an (8×8) unit cell array of single layer MoS_2, constructed with a DFT- optimized lattice parameter (a=3.18 Å). We place a sub-nanometer-sized 29-atom gold nanoparticle (Au_{29}) on this free-standing MoS_2 film to probe their catalytic activity. As elaborated in our previous work,[59] we have chosen the particular size and shape of the Au nanoparticle for computational feasibility while mimicking the shape of similar supported nanoparticles[90] and its usage in earlier computational studies.[91] 15 Å of vacuum are used to minimize interactions between periodical images in the direction normal to the surface. This Au_{29}/MoS_2 system is fully relaxed using standard techniques. We sample the Brillouin zone with one k-point at the zone center, which is sufficient for computational accuracy as the size of supercell is large (consisting of more than 200 atoms). For ionic relaxations we ensure that all components of forces acting on each atom are less than 0.01 eV/Å. Activation barriers for the reactions were found using the climbing-image nudged-elastic-band (CI-NEB)[92] method with seven configurations along the minimum energy reaction pathway.

The MoS_2 material of this study is not single-crystalline but has internal grain boundaries on the 100 nm scale;[81] their precise geometric structure can only be approximated from scanning transmission electron microscopy (STEM).[81] In order to ascertain that these grain boundaries have low impact on our results, we compare the activity of gold

nanoparticles supported at line-defect and pristine MoS_2 in our computational work. Our computational findings predict enhanced activity for gold nanoclusters on pristine MoS_2 in validation of our experimental finding.

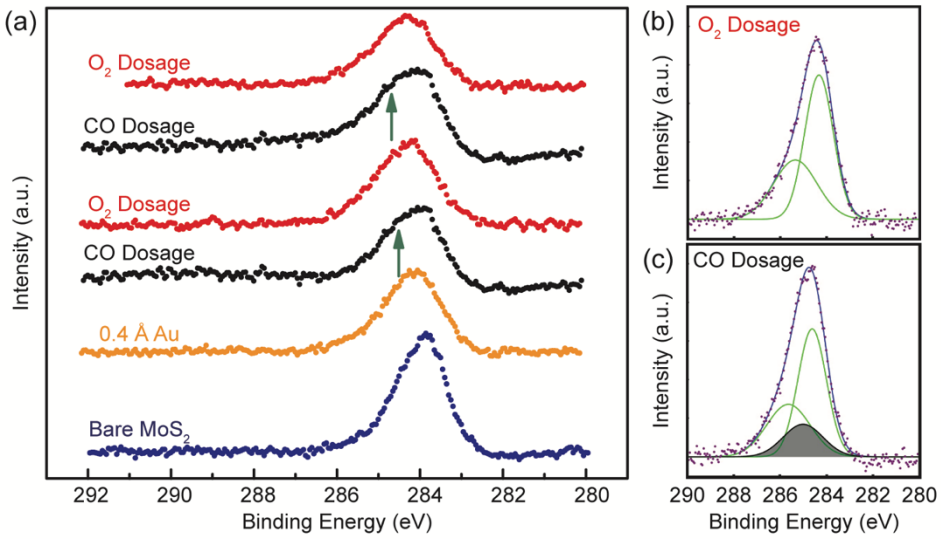

Figure 4.3(a) XPS spectra of the carbon 1s core level region of (from bottom to top) the initial MoS_2/SiO_2 substrate, after deposition of gold, after exposure to 100 L of CO, after subsequent exposure to 200 L of O_2, after subsequent exposure of 450 L of CO and finally after subsequent deposition to 110 L of O_2. (b,c) show fitting of the carbon 1s spectral features: we use two Gaussian peaks with fixed separation, relative weight and broadening to represented the feature after oxygen exposure. Using the same representation of the substrate carbon after CO exposure, a third Gaussian peak is required to fit the spectrum, which we associate with adsorbed CO.

Figure 4.3 shows a series of successively-acquired XPS spectra after subtraction of a Shirley background: from bottom to top, the preparation of our MoS_2 film results in a small amount of carbon. The combination of strong and spatially homogeneous photoluminescence signal from the sample and the absence of a carbon Raman peak[81] indicate that the observed carbon is incorporated into the substrate silica and not directly affecting the MoS_2 overlayer or gold islands. Subsequent deposition of Au into nanoscale islands on the substrate renders the carbon signature more asymmetric. We attribute this

to the different electronic environment of carbon under *versus* next to nanoscale gold islands. The effect of the gold deposition is also apparent in a shift of the Fermi level of the MoS_2 film that is visible in Figure 4.3a as the spectral offset of the carbon features before and after gold deposition. This offset has been reported earlier and evidences the charge transfer as part of the Au/MoS_2 interaction.[57]

Exposure of the gold nanoparticles to 100 Langmuir (L where 1 L [Langmuir] = 10^{-6} Torr sec of exposure uncorrected for ion gauge cross-section) of carbon monoxide causes a change of the carbon peak as highlighted by the arrow marker at the third spectrum from the bottom in Fig 4.3a. This peak corresponds to the carbon of CO molecules adsorbed on the nanoscale gold particles. Note that under room temperature no adsorption of CO on gold is expected, unless the gold is present in very small particles that through interaction/charge transfer with the substrate are activated to interact with gold.[75–77] Subsequent exposure to 200 L of oxygen (fourth spectrum from the bottom) removes this feature again. We interpret this as evidence for CO oxidation on the gold nanoparticles. The following section on computational results will provide additional details. The last two spectra show that this titration experiment is repeatable: renewed exposure to CO reestablishes the CO spectral signature in the carbon 1s peak and renewed exposure to oxygen removes it again.

Figure 4.3b,c show the a deconvolution of the C 1s feature using two Gaussian peaks in the absence of CO. Fixing the peak separation, relative intensity and peak widths, we can represent the carbon 1s feature after CO adsorption only by introducing one more

Gaussian peak (shaded) that represents adsorbed CO. Repeated presence and absence of this peak following carbon monoxide and oxygen exposure, respectively, validates the catalytic activity of gold nanoparticles on single-layer MoS_2-covered SiO_2.

Computational Results

CO Adsorption**:**

As a starting point for computational evaluation of CO oxidation on Au nanoparticles stabilized by MoS_2 we performed DFT calculations of adsorption geometry, structure and energy for CO bonded to various geometrically distinct sites of the model Au_{29} gold nanoparticle. In order to highlight any potential effect of substrate defects, we address Au_{29} clusters supported on both a pristine MoS_2 single layer (Figure 4.4a) as well as on one that is affected by a line defect (Figure 4.4b). In each case we calculated the adsorption energy at 12 distinct sites (as labelled in Figure 4.4c,d). For Au_{29} supported on pristine MoS_2 (Figure 4.4a), the strongest adsorption of CO (~1.0 eV) is found at a corner site on the cluster edge (5) at which the gold atom is coordinated with two sulfur atoms in close proximity underneath. High adsorption energies are also found directly atop the cluster (1) as well as at other corners on the periphery (7). At these sites the C-Au bond length is comparatively short at ~1.94 Å while lower adsorption energy sites also feature longer C-Au bond distances (shading in Figure 4.4c).

On Au_{29} supported on MoS_2 with a line defect (Figure 4.4b), the adsorption of CO is found to be stronger peaking at ~1.26 eV at the peripheral corner of the cluster closest to the line defect (7) and then followed by a similar corner position as found for the optimal

adsite on the Au_{29} cluster on the pristine substrate (5). The C-Au bond length is found to be 1.95Å at the optimal site on the cluster on the line-defect substrate, in good agreement with the optimal adsorption configuration on the cluster on the pristine substrate.

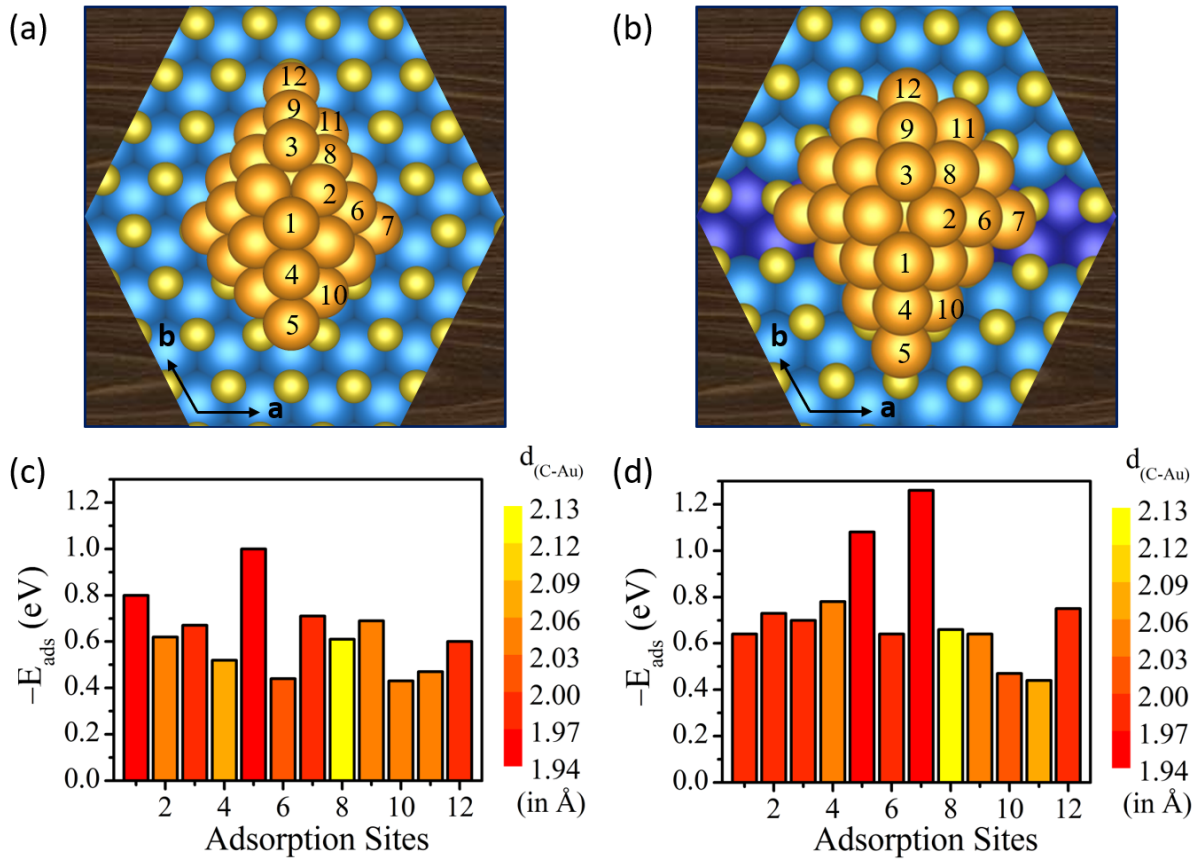

Figure 4.4 (a,b) Tested CO adsorption sites on Au_{29} nanoparticle supported on: a) pristine single-layer MoS_2; b) single-layer MoS_2 with a line defect. The blue, yellow, and golden spheres represent Mo, S, and Au atoms, respectively.; and (c, d) Adsorption energy of CO at the locations indicated in a) and b). The bar color indicates the C-Au bond length according to the scale on the right.

The adsorption energies on our gold nanoparticles are higher than those found on pristine Au and pristine MoS_2. On the latter, CO adsorption either is weak or is not energetically

favorable as indicated by prior DFT calculations (LDA functional yields ∼−0.13 eV for a configuration in which CO lies at ∼2.95 Å above MoS_2, while GGA-PBE gives +3.0 eV for one in which CO sits at ∼3.62 Å above MoS2).[93] CO does not adsorb on Au(100) as the adsorption energy comes out to be positive (0.38 eV).[94] In contrast to the extended Au surfaces, pristine Au_{29} nanoparticle displays a CO adsorption energy of −0.27 eV[91] (at a corner site), thus indicating that the nanoparticle Au sites are more reactive than the terrace Au sites. However, this adsorption energy of CO on Au_{29} is still much less than that on MoS_2-supported Au_{29} (E_{ads} ∼ −1.3 eV). As already discussed,[59] when Au nanoparticles come in contact with MoS_2, charge transfer takes place between Au and the substrate, affecting the electronic structure of the nanoparticle in a way that promotes its reactivity toward CO adsorption.

CO Oxidation Pathway**:** To determine the site-favorable reaction pathway, we performed calculations of minimum energy paths for CO oxidation at peripheral sites and at the apex of the gold nanoparticle supported on pristine and defect-laden MoS_2. Figure 4.4a and 4.4b show the computed energy profiles for the minimum energy reaction paths for CO oxidation on Au_{29} supported on pristine MoS_2 and on MoS_2 with a line defect, respectively. The lowest activation energy is found for CO adsorbed at the periphery of an Au_{29} cluster on pristine MoS_2 realizing as initial state (IS) the most favorable CO adsorption positions shown in Figure 4.4. We find the reaction to be favored by an energy of ΔE= -2.44 eV, a highly exothermic value, where ΔE refers to the difference in energy between initial and final state (FS). The computed barrier for the reaction is only ~0.28

eV and readily accessible at room temperature. Its value is only about half that for CO oxidation on Au_{24}/TiO_2 system (~0.61 eV).[8] The insets in Figure 4.5a show the computed initial state (IS), transition state (TS) and final state (FS). In a previous study we had addressed a number of reactions on such gold clusters (but not CO oxidation) and consistently found peripheral sites to be those with highest adsorption energy; this is the case here as well.

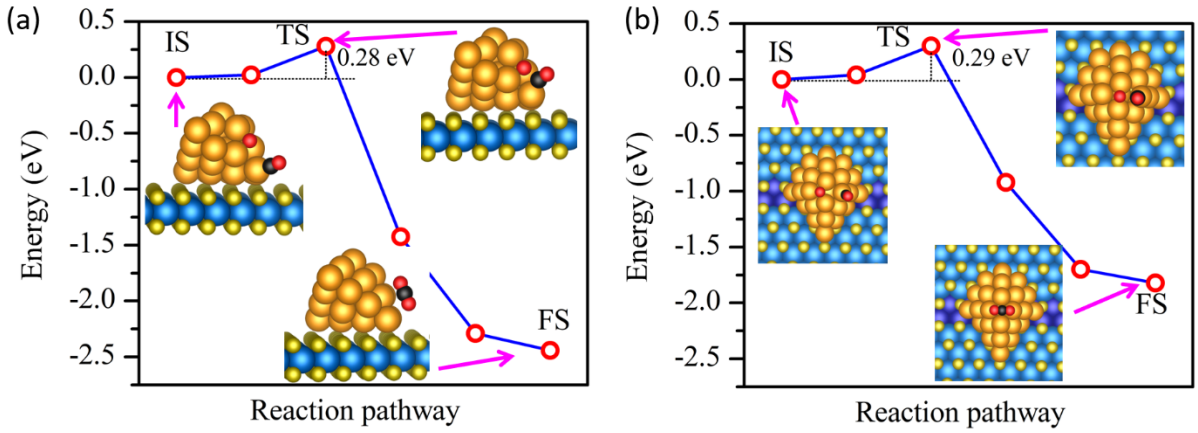

Figure 4.5 DFT calculated energetics for minimum-barrier CO oxidation reaction pathway on a) an Au_{29} cluster on pristine MoS_2 and b) an Au_{29} cluster on MoS_2 with a line defect. While on the pristine substrate the reaction occurs at the cluster periphery, on the defect-laden MoS_2 the lowest barrier is found at the cluster apex. Here, IS, TS and FS refer to the initial, transition and final states, respectively. The blue, yellow, golden, black and red balls represent the Mo, S, Au, C, and O atoms, respectively.

The CO oxidation on the Au_{29} cluster on the MoS_2 substrate with a line defect exhibits an activation barrier of ~0.29 eV, quite similar to the one found on pristine MoS_2 support. Figure 4.5b illustrates the reaction pathway. However, the minimum barrier is only found for initial CO adsorption at an apex site, and not at the location of highest binding energy of the CO adsorbate near the line defect. Computational screening of a multitude of

reaction pathways finds that CO oxidation at the peripheral location, where the highest adsorption energy of CO is found, has at minimum an ~0.09 eV higher activation barrier compared to the apex site. We attribute this to the strong initial binding of the CO molecule in initial state (IS) on the defect-laden MoS_2 that needs to be overcome to reach the transition state (TS).

These findings point to the possibility that defect-laden MoS_2 is actually unfavorable for supporting gold-based CO oxidation compared to pristine MoS_2. In this context we highlight that the combination of STEM data on the crystallinity of our MoS_2 film[81] and the SEM data on the gold island distribution (Figure 4.2) confirm that the overwhelming majority of the gold islands in our study are located on pristine MoS_2.

Conclusion

Deposition of a single-layer MoS_2 film onto an inert oxide substrate renders it capable of stabilizing gold as nanoparticles catalytically-active for CO oxidation at a very low reaction barrier of ~0.3 eV. Such a barrier is readily accessible even at room temperature and only about half that found computationally for Au/TiO_2. A deposition method for arbitrary-thickness integer-layer MoS_2, initially developed for electronic applications, was able to provide MoS_2 single-layer films at sufficient homogeneity and length scale that lab-based x-ray photoelectron spectroscopy with a beam spot of about 1 cm^2 was able to determine repeated CO binding and release of the oxidation product at room temperature.

4.3 Methanol Carbonylation to Acetaldehyde

The following chapter contains excerpts from "Towards Higher Alcohol Formation using a single-layer MoS_2 activated Au on Silica: Methanol Carbonylation to Acetaldehyde" by K. Almeida et. al.

The formation of higher alcohols from syngas is an important goal in the quest for economic and sustainable transformation of biomass into transportation fuels.[95] A necessary step for its realization is efficient C-C coupling involving oxygenate small molecules such as carbon monoxide and methanol.[96,97] Important work by Haruta *et al* showed that CO oxidation is catalyzed by supported nanoscale gold particles.[48] This showed that the catalytic activity of metals that are relatively inert in the bulk can be enhanced through nanostructuring.[49] In recent work,[59,98] we have shown that single-layer molybdenum disulfide (MoS_2) coating can transform an otherwise inert substrate, silica, into a catalytic active surface for CO oxidation by gold nanoclusters. This is similar to results obtained on reducible oxides, such as titania and ceria.[50–56] Concomitant computational efforts have predicted a number of feasible, low-barrier reaction pathways on thus supported gold nanoparticles,[57,59] in contrast to the catalytically largely inactive bulk gold, gold on pristine silica, or on other 2D materials like graphene.[58,60,61] Here, we address the carbonylation of methanol as the most fundamental C-C coupling step that can lead to higher alcohol formation from a lower alcohol. The mixture of methanol and carbon monoxide was investigated as an approximation of the reaction stream from syngas over the catalysts surface; hydrogen, water and other species were excluded to maintain a system

simple enough to model computationally. Syngas may be obtained from biomass gasification and conversion to higher alcohols is a potential rapid pathway toward sustainable and renewable fuels.

Molybdenum disulfide has been investigated for a wide range of catalytic applications. MoS_2 with cobalt and alkali modifiers is the key catalyst material in industrial hydrodesulfurization; notably, the industrial catalyst material resembles a few-layer film of supported MoS_2.[62] Alkali modification of this material has also been proposed for alcohol formation.[63,99–106] The mechanistic aspects of these studies have been focused on the hydrogenation step, in particular the initial CO hydrogenation to produced methanol. To further the understanding of catalysis over this material, our study focuses on the extension of the carbon chain (Figure 4.6a) toward higher alcohols through the carbonylation of methanol.

MoS_2 has gained prominence as a catalyst for hydrogen evolution;[65,66] its activity has been attributed to edge sites based on low-temperature measurements,[67] and related materials that feature large number of exposed edge sites have been prepared and validated in some catalytic applications.[68–74] In such a configuration MoS_2 edges are the catalyst. We sought to investigate the interaction between the support and catalytically active nano clusters. By producing polycrystalline continuous single-layer MoS_2 coatings over several centimeter in diameter,[81] we avoid the activity of edge sites and can focus solely on grain boundaries and metal-MoS_2 sites. This simplified structure allows us to probe the fundamental chemistry of chain lengthening.

Surprisingly, the carbonylation of methanol was catalyzed over the Au-MoS_2 structures to yield acetaldehyde. Using a laminar flow reactor, acetaldehyde formation occurred at fairly low temperatures (as low as 393 K), on single layer MoS_2 films, decorated by nanoscale gold islands. Density functional theory (DFT) modeling was used to find a plausible pathway for this important carbon-carbon coupling step.

Experimental

A Ø1.5 cm x 1 mm thick fused silica window (Esco Optics) was homogeneously coated

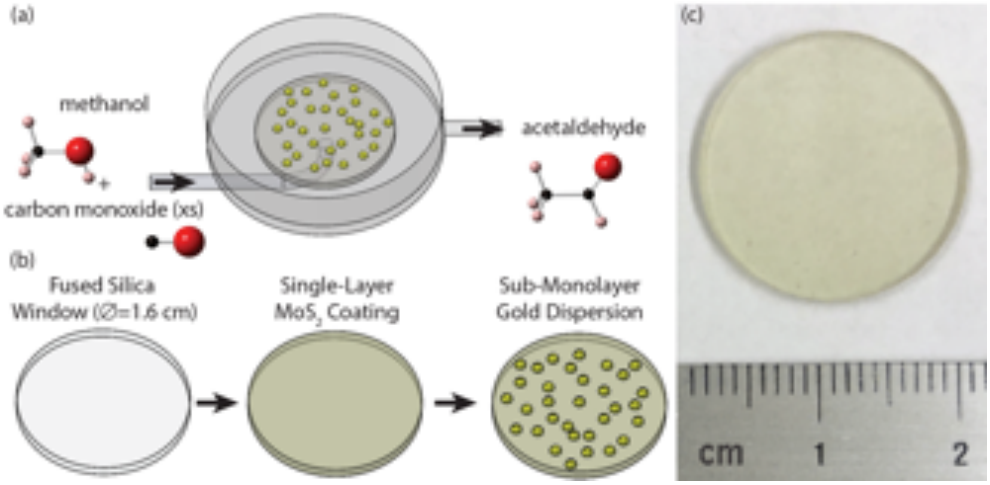

Figure 4.6 a,b) Schematic representation of the catalyst preparation and catalytic evaluation in a laminar flow reactor; c)The Ø1.5 cm fused silica window coated with a single-layer of MoS_2 and deposition of gold exhibits a yellowish color.

with a single polycrystalline layer of MoS_2 decorated by nanoscale gold islands corresponding to an average gold coverage of 0.5 Å, 1Å, and 2Å or approximately 1/6, 1/3, and 2/3 of a monolayer respectively. Figure 4.6b shows the preparative effort schematically and Figure. 4.6c depicts the fused silica window after single-layer MoS_2 and gold deposition.

To make the supported catalysts, we have utilized a technique for coating inert oxides by an MoS_2 films of controlled integer layer number, as reported elsewhere.[81] The original work focused on MoS_2 films on a dry oxide SiO_2 layer on a silicon wafer substrate. The single- and few-layer MoS_2 growth technique is based on heating molybdenum filaments to white heat (>1500 K) under high vacuum followed by exposure to carbon disulfide. Decomposition of the disulfide on the Mo filament surface results in volatile MoS_x precursors, which are precipitated onto the substrate. The substrate is held at a temperature where MoS_2 island growth and desorption is at equilibrium. Reference sample for scanning electron microscopy were prepared on a thin (30 nm) silicon dioxide film on a doped silicon substrate. Gold was deposited with an e-beam evaporator monitored by quartz crystal microbalance. Deposition rates were calculated from the measured mass increase and converted to Ångstroms of gold per minute. Values below the atomic diameter of gold (3.2 Å) indicate incomplete (sub-monolayer) coverage and cluster formation.

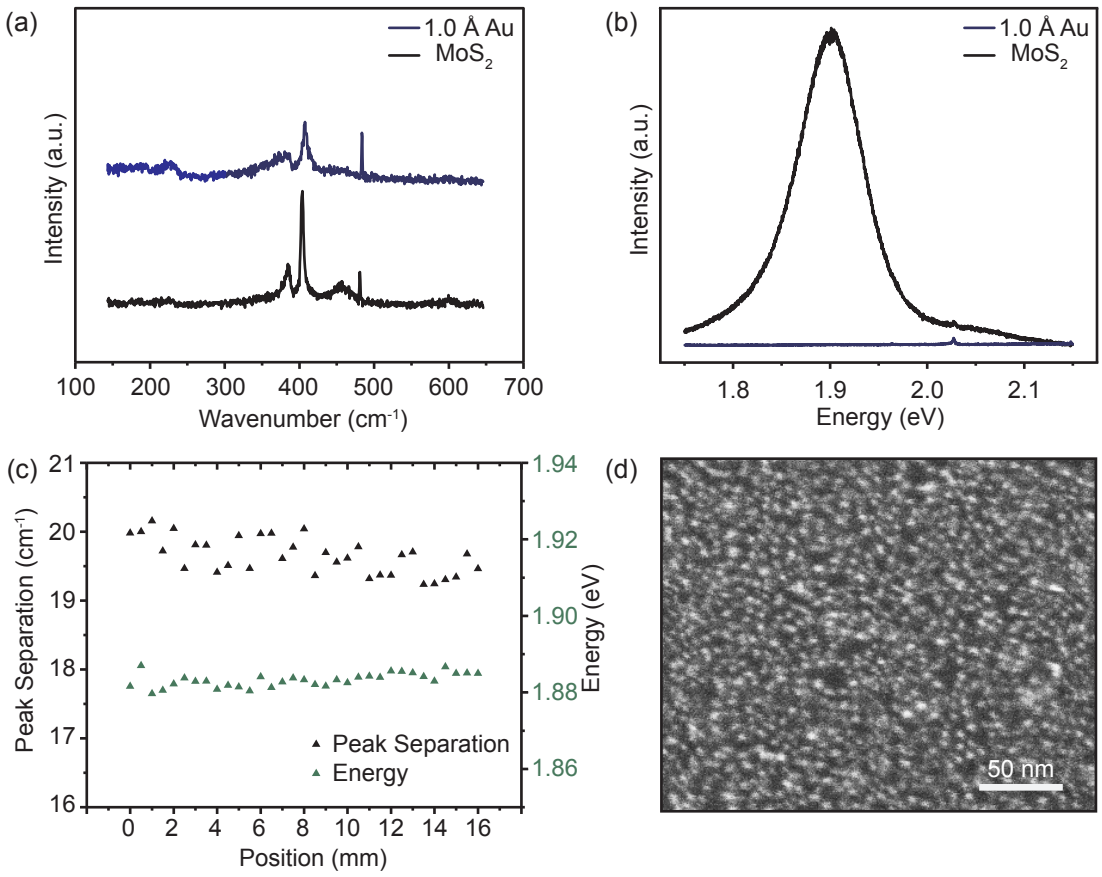

Figure 4.7 The (a) Raman and (b) photoluminescence spectra of a single-layer MoS_2 sample before (black) and (color) after sub-monolayer gold deposition. (c) homogeneity of the single-layer MoS_2 film across the fused silica substrate; Raman A_{1g} - E_{2g} peak separation and photoluminescence position were mapped along the dashed horizontal line of Figure 4.6c. (d) SEM image of Au dispersion across the top of a single layer MoS_2 film on a 30nm silica test film. A homogeneous distribution of gold clusters each smaller than a few nanometers was observed.

The samples exhibit (Figure 4.7a) the typical Raman peak positions for single-layer MoS_2 films for E_{2g} and A_{1g} at 385.5 cm^{-1} and 404.9 cm^{-1} (separation 19 cm^{-1}).[82] Before gold deposition, the photoluminescence of the substrate material was intense and centered at 1.91 eV with a full-width at half-maximum of ~0.1 eV, the optical bandgap of single-layer MoS_2 (Figure 4.7b).[3,4] After gold deposition, the photoluminescence is quenched. This indicates that despite the incomplete surface coverage, there is a quenching center within

the size of practically any exciton created on the surface. This suggests efficient dispersion of gold on MoS_2/SiO_2, in contrast to gold on bare silica or graphene. Direct scanning electron microscopy (SEM) imaging of a test sample with a 30 nm silica film on silicon shows tiny, point-like gold particles below the limit of the instrument's resolving power (Figure 4.7d). These particles are a maximum of 1-3 nanometers in size, i.e. in critical size range for catalytic activity.[75–77] The spatial homogeneity of the sample was verified by determining the Raman peak separation and photoluminescence position along a line across the substrate (Figure 4.7c).

Reactor studies were performed in a laminar flow reactor. The goal of this study was to determine the chain lengthening products from carbon monoxide addition to methanol. To this end reactions were run for 140 minutes. This allowed the product composition to stabilize and be analyzed in steady state. Product analyses were performed on two gas chromatographs: an Agilent 6890 with a wax column (Restek Stabilwax, 30 m, 0.32 mm ID, 1.0 μm film thickness) and a mass sensitive detector (Agilent 5973) was utilized for samples taken with a 25 mL gas tight syringe from a sampling port in the product stream. An Agilent 6850 gas chromatograph with a wax column (Restek Stabilwax, 30 m, 0.32 mm ID, 1.0 μm film thickness) and thermal conductivity detector (TCD) was connected directly to the product stream via a transfer line and a gas-sampling valve. The chromatographic methods and the laminar flow reactor are further described in the supplementary material. Blanks were run with an empty reactor, with a blank silica substrate, and a MoS_2 coated substrate with no gold.

Results

Acetaldehyde Production

The reactant stream consisted of CO gas at 308 kPa bubbled through a methanol reservoir at 20 ˚C. At this temperature methanol has a vapor pressure of 13 kPa or 4.2% of the feed stream. Prior to the reaction, the reactor was purged with argon gas and heated to the reaction temperature of 120°C. After 120 minutes on stream a sample was taken for GC-MS analysis by a sampling port. Comparison of the product peak with GC-MS chromatogram of a standard acetaldehyde/methanol mixture indicated the observed peak in the TCD chromatogram is acetaldehyde.

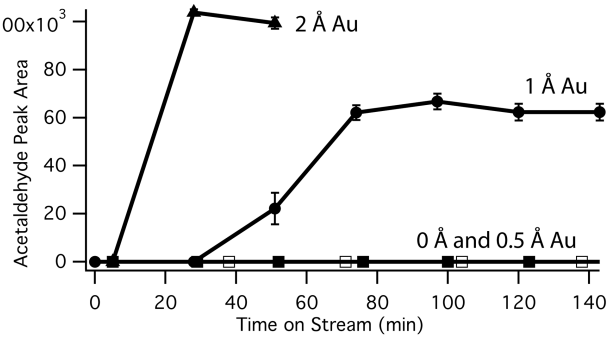

Figure 4.8 . Integrated acetaldehyde peak intensity using thermal conductivity detection as a function of the on-stream time of the catalyst showing onset of activity starting at 30 min on stream. Time zero is when the reactor, at temperature, was switched from an argon feed to reactant.

Carbon monoxide (RT= 2.295 min), acetaldehyde (RT=3.305 min), methanol (RT=4.245 min) and water (RT=5.149 min) were detected in TCD chromatograms. Water was detected in all reactions (with and without gold) at very low concentrations.

We explored the stability of the catalyst by running the reactor for 140 minutes and reusing a catalyst after on stream. The 1Å catalyst was utilized for 140 minutes, stored in an Ar-filled glovebox for 20 days and reused. Catalytic acetaldehyde formation was still observed. Figure 4.8 shows the production of acetaldehyde as time on stream for all samples. While we observe a slight drop initially, we find that subsequently the reaction

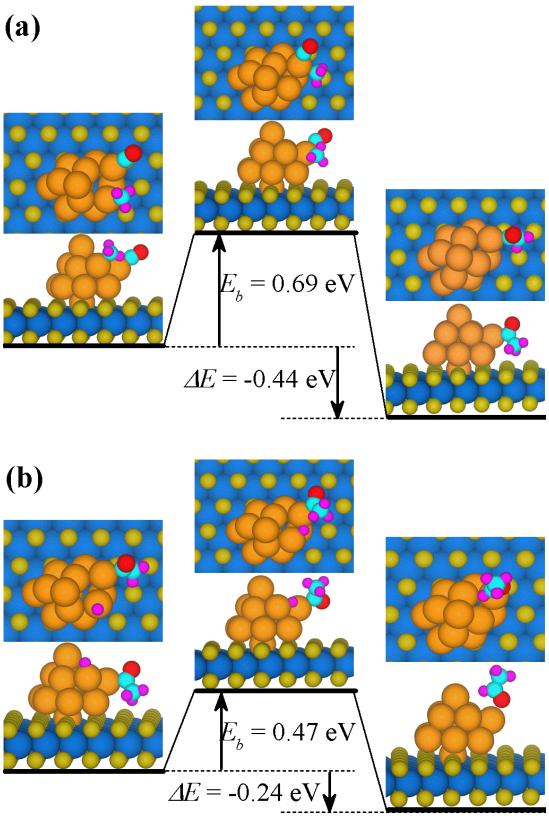

Figure 4.9 . Reaction pathways of CH_3* + CO* → CH_3CO* (a) and CH_3CO* + H* → CH_3CHO* (b). Left, center, and right images show both top and side views of initial, transition, and final states, respectively. Blue, yellow, gold, cyan, red, and magenta balls represent Mo, S, Au, C, O, and H atoms, respectively. E_b and ΔE are activation barrier and reaction energy, respectively.

proceeds at a consistent rate. The delay in the onset of catalysis is related to the flow rate of the reactant stream. This is the time to purge the 13.4 cm^3 transfer line volume when switching from argon purge to reactant stream. The 2 Å sample had a higher reactant flow rate. In order to determine the origin of the observed reactivity, we also investigated the same reaction using a blank consisting of the MoS_2 coated substrate without gold. We did not observe the formation of acetaldehyde on this sample.

Density Functional Theory-Based Evaluation

Accompanying density functional theory (DFT) calculations validate the feasibility of the formation of carbon-carbon bonds at the surface of MoS_2-supported Au nanoparticles from carbon and methanol alone. Continuing the success of previous computational work,[107] in which the alcohol synthesis from syngas (CO and H_2) was shown to be favorable on Au_{13} nanoparticles stabilized by interactions with a single layer of MoS_2, we use the same supercell setup to study the formation of a bond between adsorbed methyl and carbonyl species to acetyl. Our DFT calculations are based on the plane-wave basis set

and the pseudopotential method employing the generalized-gradient approximation (GGA) in the form of the Perdew-Burke-Ernzerhof (PBE)[108] functional together with DFT-D3 correction[109] to take into account the electron-exchange interaction including van der Waals interactions. Transition states and activation barriers reactions are calculated using the climbing-image nudged elastic band (CI-NEB) method[49, 50]. Further details of the calculations can be found in previous work.[107] We consider the formation of acetaldehyde by study the most likely processes: CH_3* + CO* → CH_3CO* and CH_3CO* + H* → CH_3CHO*, where CH_3* and H* species are produced through the adsorption and dissociation of methanol on the stabilized gold surface (* designates adsorbed species). Additional CO is required to reduce residue O* species via O* + CO*→ CO_2*, a highly exothermic reaction (ΔE = -2.23 eV) with a barrier of 0.06 eV, as also described elsewhere.[59,98] Figure 4.9a,b shows the initial state, transition state, and final states of the CH_3* + CO* → CH_3CO* and CH_3CO* + H* → CH_3CHO* reactions. Our calculations indicate that the formation of a bond between the adsorbed CH_3* species and a CO* molecule on Au_{13} is energetically favorable as the reactions are exothermic and the activation barriers comparatively low: 0.69 eV for the acetyl formation (I) (Figure 4a) and 0.47 eV for the hydrogenation of acetyl to acetaldehyde (II) (Figure 4.9b). The resultant CH_3CHO* is desorbs with a desorption energy of 0.45 eV.

Close inspection reveals that site with the lowest pathway barriers corresponds to the least coordinated gold atom on the cluster, where the binding of the reactants is strongest. Such sites are far more common on small gold clusters. This finding highlights the importance

of small clusters for this reaction to proceed. Single-layer of MoS_2 serves to provide a surface where dispersal of gold into nanometer-scale clusters is favorable.[57]

Conclusions

The deposition of gold nanoparticles on a single layer of MoS_2 on an inert fused silica substrate provides a surface capable for the carbonylation of methanol to acetaldehyde. This result showcases the promise of gold nanoparticles single layers of MoS_2, discussed elsewhere.[49] This work provides understanding of alcohol chain lengthening reaction over MoS_2 supported catalysts. The possibility of extending this reactivity to produce higher alcohols is predicted from our DFT calculations.[48,97] Our findings highlight an important first step towards the formation of higher alcohols from methanol or even syngas using thin layers of MoS_2 and less than a monolayer of gold. We show that a non-active support such as silica can be converted into an active support though the application of single layers of active support. Although, MoS_2 is a commodity mineral, it is limited in occurrence. We show that a very small amount of MoS_2 is required to produce an effective catalyst. A monolayer on 2 mm beads would be an equivalent MoS_2 loading of 1.88 ppm and an Au loading of 1.15 ppm. A cubic meter of supported catalyst prepared in such a way would require 146 mg of MoS_2 and 90 mg of gold. The low reaction temperatures and pressures (308 kPa and 393 K) further support the appeal of this approach. Additionally, acetaldehyde can be oxidized to acetic acid yielding a route to acetic acid without the need for iodides. Although the basal plane of MoS_2 is inert edge sulfur vacancies are thought to key to hydrodesulfurization and hydrodenitrogenation activity over MoS_2.[110] Our results illustrate a mechanism by which the basal plane and grain boundaries can influence the

chemical activity of a metal catalyst. Furthermore, our results also speak to sustained reactivity of Au nanoparticles in a scenario in which inert substrates can be first shaped into desired structures that optimize reactant and heat flow and serve as an inexpensive scaffold for a composite that bestows catalytic activity on them.

Chapter 5: Optimization of the MoS_2-GaN Interface

5.1 Motivation

Gallium nitride is an excellent semiconducting material with a wide band gap at 3.4 eV. For further application in electronics, many look to integrate 2D materials for heterostructure diodes. MoS_2 is a desirable semiconducting material and it is found to have an excellent lattice match (mismatch of ~0.8% at RT) with GaN,[111] thus, avoiding any drops in performance that may arise due to mismatching. This structure has application in electronics and optoelectronics such as broadband photodetection.[112]

It is reported that depositing MoS_2 on GaN can be difficult due to the emergence of a dirty layer in between the two materials thereby having the potential to negatively affect the device performance.[113] The high vacuum growth reactor is used in order to avoid these difficulties by successfully cleaning the substrate surface prior to film deposition. We perform this technique strictly in high vacuum to maintain a clean interface, only opening to atmosphere when removing the finished sample for further characterization.

5.2 GaN Reference Characterization

Prior to analysis of the MoS_2/GaN heterostructure, we first characterize the reference GaN samples. Several spot checks are made across the GaN in LEED to verify the crystallinity of the purchased GaN wafer. The GaN stack used for this study is 300 μm n-GaN ($2.5x10^{17}$ cm^{-3} doping), 700 μm n-GaN ($1x10^{18}$ cm^{-3} doping), and 3900 μm i-GaN and buffer layer on p-type Si purchased from NTT-AT. The substrates are cut to 5x10 mm. We use LEED initially, to validate the crystal quality of the purchased material.

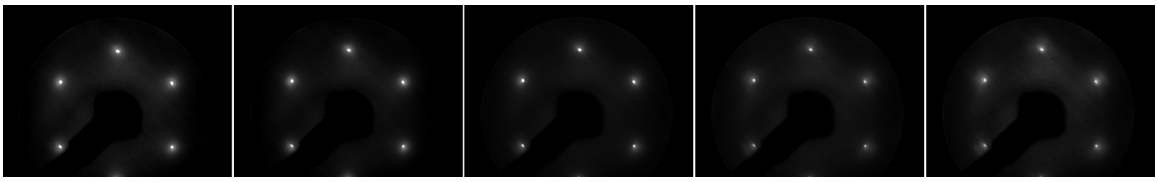

Figure 5.1 LEED images at 100 eV of the GaN reference substrate.

Figure 5.1 displays five spot checks acquired at one end to the other end of the sample located at approximately 0.5, 2.5, 5.0, 7.5, and 9.5 mm respectively. These images were acquired at 100 eV, for direct comparison to the LEED of the MoS_2/GaN shown later in chapter 5.4. This confirms the hexagonal nature of the gallium nitride and good crystallinity given the sharpness of the LEED spots. We proceed to characterize the sample further via X-ray photoelectron spectroscopy.

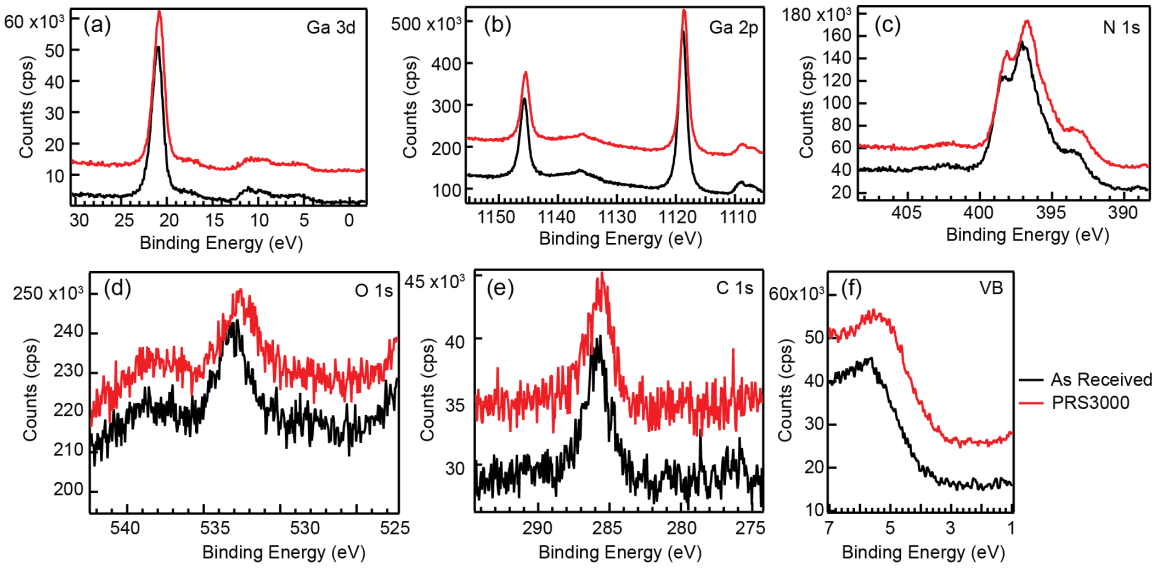

Figure 5.2 XPS measurements of the (a) Ga 3d, (b) Ga 2p, (c) N 1s, (d) O 1s, and (e) C 1s core levels of an as received and PRS 3000 cleaned sample. (f) Scan of the valence band.

The GaN reference sample is cleaned via the photoresist stripper, PRS3000. The sample that is designated “as received” was cut and not cleaned straight out of the wafer carrier.

The sample is also evaluated in XPS for the as received GaN as well as the PRS3000 cleaned. There does not seem to be much variation in the C 1s (figure 5.2d) and O 1s (figure 5.2e) core levels from sample to sample. This indicates that this cleaning technique does not seem to result in a cleaner sample as the carbon and oxygen content does not seem to be reduced. It is also apparent that there is not much of a shift from any of the core levels, including the images from figure 5.2a-c. Although there seems to be a clear shift in the valence band in from around ~3.3 eV to around ~3.2 eV that results from cleaning the GaN substrate in PRS3000.

Overall, the received GaN seems to be in good quality from the LEED and XPS measurements. We look to incorporate other techniques for the surface treatment such as an ion sputtering and annealing process.

5.3 GaN Surface Treatment and MoS_2 Deposition

We investigate the incorporation of an ion bombardment source (Varian) for a light cleaning treatment. This will be coupled with an annealing step in ammonia after the sputtering is performed. This step is to account for any nitrogen deficiency that may result from sputtering.[114] This is also reported when Zhang et. al performed a nitridation of the GaN surface via NH_3/Ar plasma treatment which resulted in a cleaner surface morphology.[115] Although this method is performed by others, it was not coupled with an initial sputtering step. Due to the destructive nature of sputtering, we look to find a balance so that we do to not induce too much surface damage to our GaN. For this reason, we

choose to use this treatment over a certain degree of sputter fluences creating a "sputter gradient" along the length of a GaN substrate.

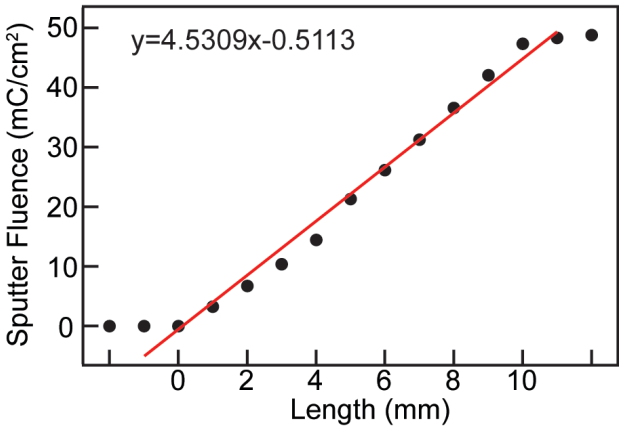

Figure 5.3 The measured sputter fluence of the Ne^+ beam as a function of the distance exposed on the substrate.

A molybdenum foil shutter was added above the sample for cover from the sputter beam as shown in figure a. Prior to the surface treatment, the GaN/Si substrate was cut to size (~5x10 mm) and was cleaned using a successive acetone, IPA, and DI water rinse and immersed in a piranha solution (10 mL H_2O_2/30 mL H_2SO_4) for 5 min. The sample is then rinsed and transferred to the chamber, placed underneath the shutter, and pumped down to 10^{-7} torr. Once the pressure is steady at $1x10^{-7}$ torr, the background neon gas is set to $1x10^{-4}$ torr for the surface treatment. Neon is used for this treatment due to its similar mass to the contaminants. The beam energy is set to 800 meV and the emission current at 20 mA. The sputter fluence of the ion sputter beam is measured using a Keithley 2400 SourceMeter in a separate experiment and is plotted in Figure 5.3. This plot shows the evolution of the sputter fluence as the shutter is withdrawn more and more. Once the entire substrate is exposed to the beam, it maxes out at approximately 45 mC/cm^2. The shutter is pulled back using a z-manipulation attachment to partially expose the GaN to the beam. It is drawn out over the length of the substrate for 5 min and turned off, Ne flow shut off. Right after

exposure to the beam, the sample is annealed at 750°C for 15 min with a background of NH_3 set to 10^{-4} torr. After the in-situ surface cleaning of the GaN is performed, the sample is cooled to 650°C, NH_3 flow shut off, and growth proceeds to cap the sample in multilayer MoS_2. This growth process is referenced in chapter 2.1.

Due to the destructive nature of sputtering, a LEED study was performed. This is also used to directly compare to the initial results from the GaN reference. LEED also provides better resolution than XPS, as the beam spot size is much smaller. Supplemental Raman, XPS, electrical measurements, and AFM is also provided to further validate the structure.

5.4 MoS_2/GaN Characterization

The described experimental process in chapter 5.2 is shown in figure 5.4a. Each arrow indicates different steps that occur during each run: initial formation of the sputter gradient, subsequent NH_3 anneal and MoS_2 deposition. It is believed that due to the anneal in NH_3, the surface of gallium nitride is nitridated.[115] This nitridated surface with stacked MoS_2 is shown in figure 5.4b. From figure 5.4b, we can see the nitrogen naturally buckle resulting in the 2x2 structure observed. The gradient is first analyzed via Raman spectroscopy. Figure 5.4c,b shows spectra of a multilayer MoS_2 sample (~24 cm^{-1} peak separation) on gallium nitride. This peak separation of 24 cm^{-1} corresponds to multilayer MoS_2.[82]

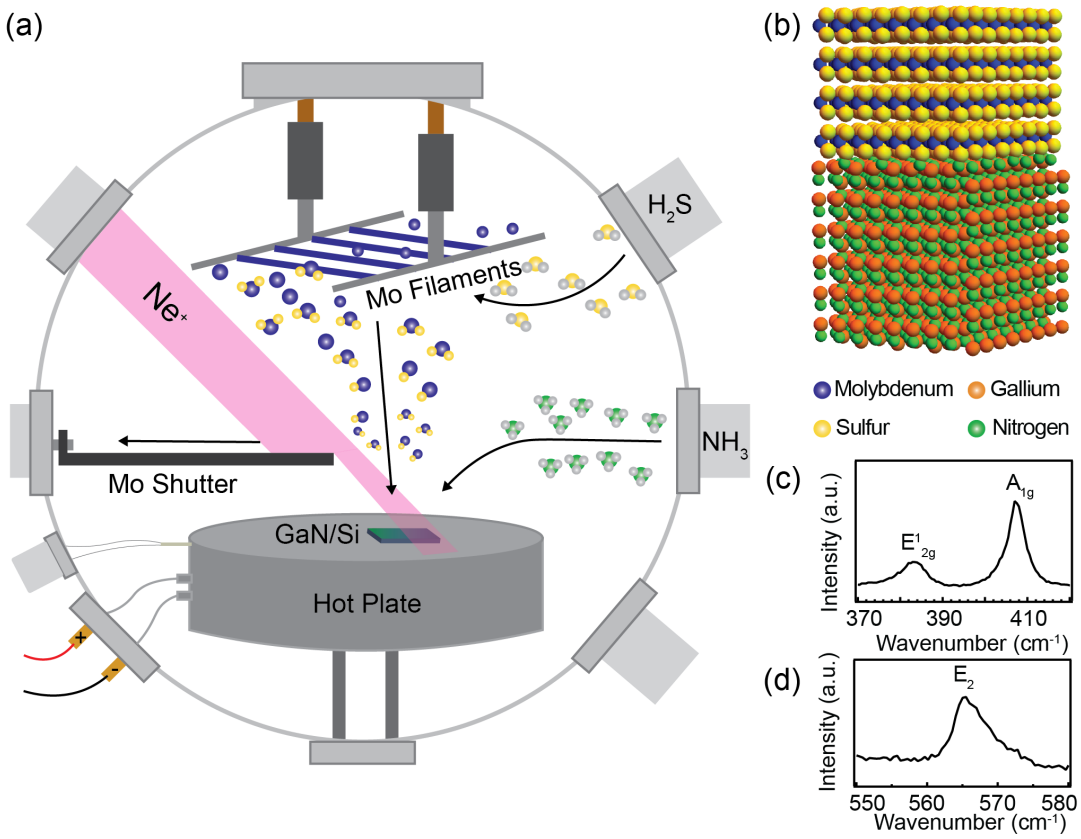

Figure 5.4 (a) Schematic representation of the growth and MoS_2 deposition process. (b) Stacked atomic structure of MoS_2/GaN. Raman spectra of the (c) E_{2g}, A_{1g}, and the (d) E_2 (high) Raman modes for multilayer MoS_2 on GaN.

This sample structure is also evaluated by LEED. These measurements are performed at $1x10^{-9}$ mbar. A LabView program was created to take an array of images at different spots on the sample using an Arduino board and x- and y-stage motors. Each step was approximately 572 μm for the first 12 steps and 134 μm thereafter. This resulted in the acquisition of 44 total steps along the entirety of the substrate. At each step the beam energy was measured from 80-300 eV to evaluate the MoS_2/GaN interaction at the surface and deeper into the sample.

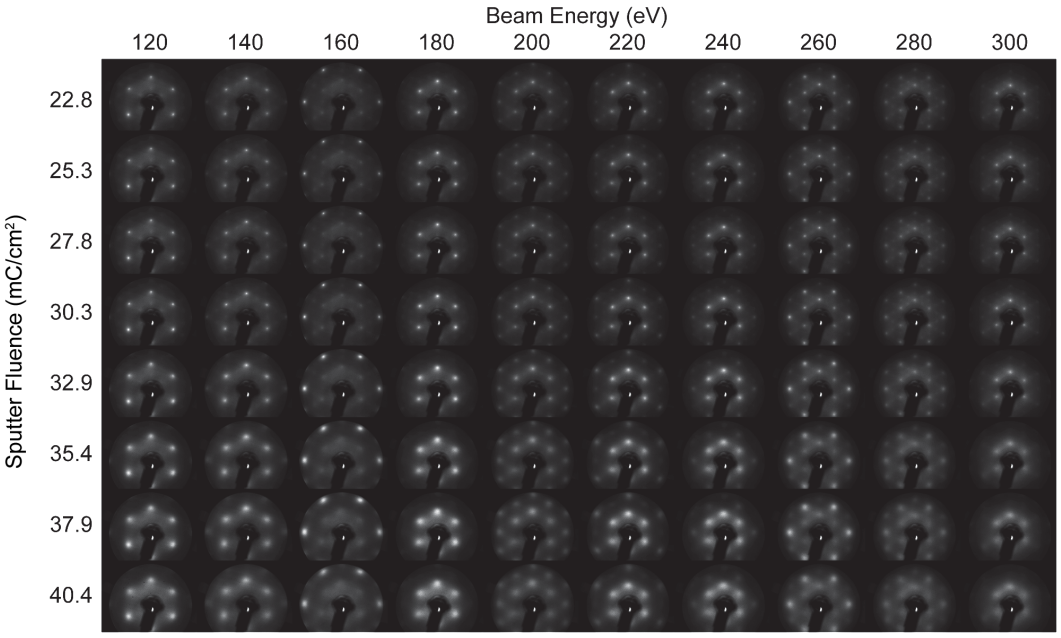

Figure 5.5 LEED images acquired at 120-300 eV with the sputter fluence in the range of ~20-40 mC/cm^2.

As the beam energy is increased from 120 eV to 300 eV, a 2x2 reconstruction of the underlying GaN is observed within certain regions of the sample. The array of images in Figure 5.5 shows the evolution of the 2x2 reconstruction as the sample undergoes more sputtering. The 2x2 reconstruction emerges around 10 mC/cm^2 which we can see by the doubled periodicity. This disappears around 33 mC/cm^2, believed to be due to the intensity of the sputter beam thereby creating a rough GaN surface. This provides further confirmation of the near 2D nature of the MoS_2, given that LEED is primarily a surface characterization technique. This implies that there is no contamination layer in between the interfacing layers at this region of the sample.

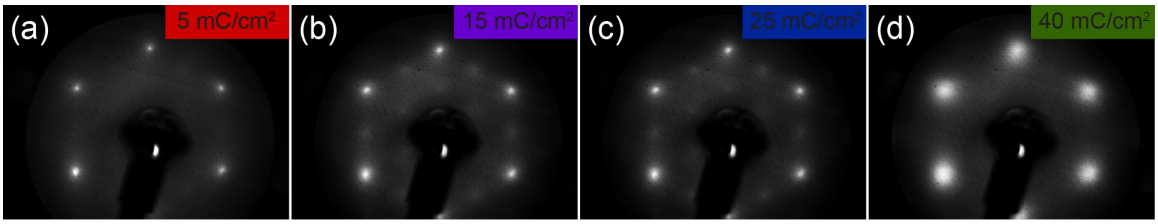

Figure 5.6 LEED images at 100 eV showing the (a) 5 mC/cm^2, (b) 15 mC/cm^2, (c) 25 mC/cm^2, and (d) 40 mC/cm^2 sputtered regions

The next set of images were evaluated at 100 eV, as shown in Figure 5.6. We use this set of images for evaluation due to the clear doubled periodicity. The evolution of the LEED spots can be seen in figure 5.6a-d. Initially, we see a pattern that is characteristic to MoS_2/GaN. Due to the lattice matching of the MoS_2 on the GaN, the same pattern as seen in chapter 5.2 is shown at 5 mC/cm^2. As the sample is sputtered more, the 2x2 reconstruction is observed, shown in figure 5.6b,c. This structure is believed to be indicative of the nitridated surface that resulted from the respective sputter fluence coupled with the ammonia anneal. As the sample is sputtered more, we observe the pattern shown in figure 5.6d which results after a sputter fluence of 35 mC/cm^2 and above. This image displays disordered growth atop the GaN substrate as the spots are much wider. From this data, we find that the optimal sputter fluence is in the range of ~10-30 mC/cm^2. This range corresponds directly to where the 2x2 reconstruction emerges (the nitridated GaN surface) and the sharpest peaks.

The sample was also analyzed via x-ray photoelectron spectroscopy. The samples were calibrated by scanning annealed silver foil. We analyze the sample across the length of the substrate due to the nature of the sputter gradient. The sample is mounted in the XPS

system ($6x10^{-9}$ mbar during scans) where it is connected to an x-, y-, z-stage which is used to characterize the sample across the gradient. We use a pass energy of 100 eV for the measurements and an Al (k-alpha) anode with the x-ray gun at 10 kV and 5 mA emission current.

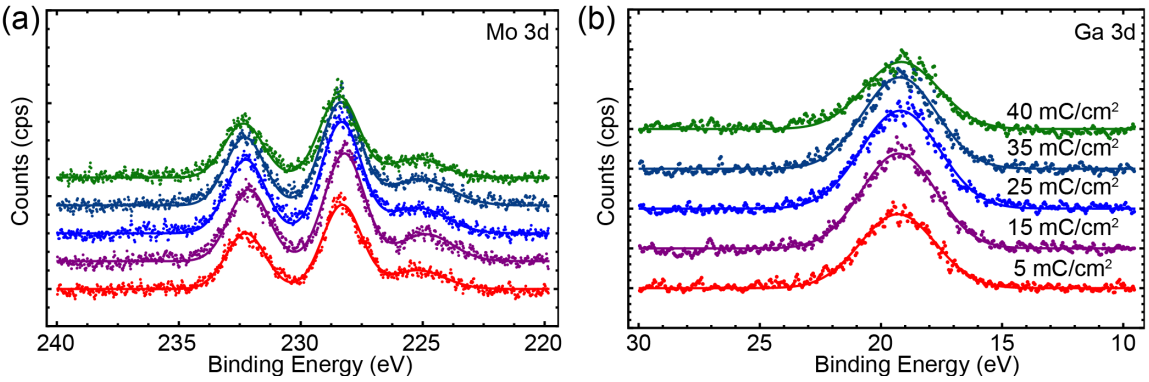

Figure 5.7 (a) Mo 3d core level and (b) Ga 3d core level of a multilayer MoS_2/GaN sample.

These peaks were fit using a Mathematica code that provided a Shirley background. The scans were taken across the sample and are appropriately labeled in figure 5.7b. It is noted that in figure 5.7b the gallium peak is not disturbed and the peak is stationary throughout the sample. We use this to reference to shifts in the Mo 3d core level. In figure 5.7a, there is a clear shift in the 15 mC/cm^2 toward lower binding energies. This results in a less disturbed MoS_2 given that the peak is shifted toward lower binding energies rather than higher. It is then implied that the valence band is shifted closer to the fermi level in this case. In the other material grown on the sputtered surface, there is a

shift to higher binding energies making this material more n-type. It is noted that the n-type nature of MoS_2 is typically attributed to the sulfur vacancies in the material.[73,116]

The thick sample was prepared as a sputter gradient to evaluate the electrical properties as a function of the sputter fluence. Once the chip was finished, it was first spun coat in 600 nm of C5 PMMA. Figure 5.8 illustrates the device fabrication process. The GaN pads were exposed by EBL, developed in MIBK, and transferred to UHV ($5x10^{-9}$ mbar) to sputter away the MoS_2. The chip was exposed to $5x10^{-6}$ mbar Ar^+ for 5 min with a filament current of 2.6 A, electron energy of 120 eV, emission current of 10 mA, and the energy source at 3 kV.

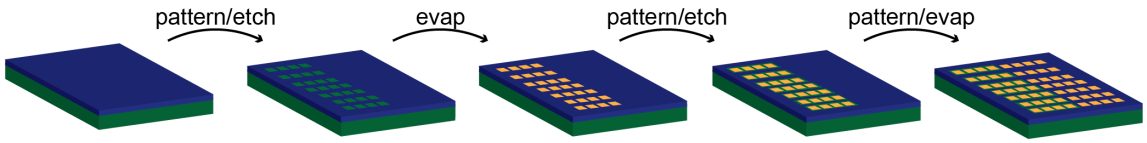

Figure 5.8 A schematic of the process flow for the device fabrication.

The MoS_2 and some underlying GaN is then etched away. The pads were fabricated by e-beam evaporation of 10 nm Ti/50 nm Al/50 nm Au. We use this stack in order to create ohmic contacts for the n-GaN.[117] After the contact material is lifted off, the area around the GaN pads is exposed and etched by the same Ar^+ to isolate the Ti/Al/Au pads. The sample is spun coat again in C5 PMMA and four MoS_2 pads are fabricated adjacent to the GaN pads with a stack of 10 nm Ti/100 nm Au. Each pad has a size of 80 μm across and are separated by 40 μm (GaN and MoS_2 pads.)

The transport properties of the device are then evaluated once the final structure is produced. Figure 5.9a shows the IV properties of the isolated GaN to GaN contacts. This shows that there is not much variation in the devices from 6.6-37.4 mC/cm^2 due to the Ar^+ etching through the MoS_2 and into the GaN, all displaying linear behavior on the order of ~25-30 µA.

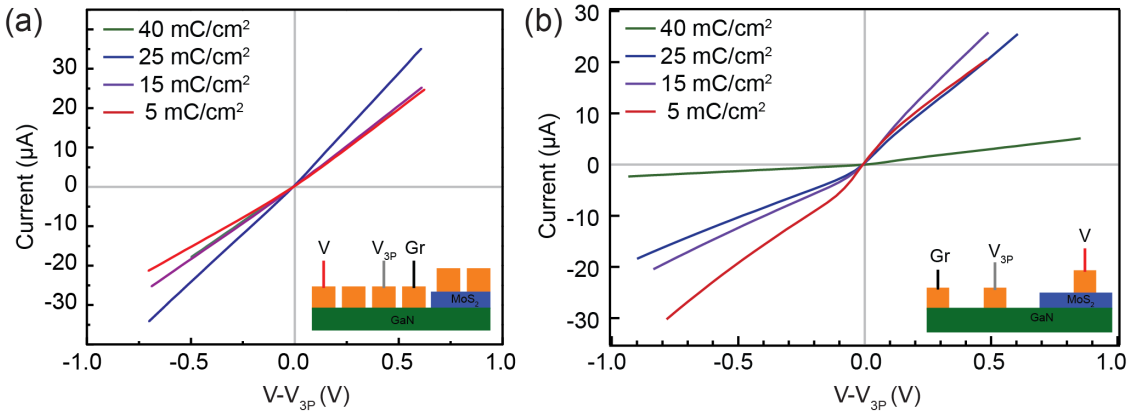

Figure 5.9 IV measurements for the (a) GaN contacts only and for (b) the MoS_2/GaN diode.

For evaluation of the MoS_2/GaN interface, the inset in figure 5.9b shows the schematic for the channel measured. The GaN is used as ground while the MoS_2 is source, based on the band structure of the n-n diode and the conduction band offset (CBO) between the two n-type materials.[112] In the forward bias, there is a higher current output of up to ~25 µA for the 15 mC/cm^2 device at 400 mV. The most sputtered device produces the lowest amount of current. It is believed that this is due to the destructive nature of sputtering which results in the disordered growth of MoS_2 along the top of the GaN substrate. The other devices are also showing weaker current-rectifying behavior with more/less sputtering. As the substrate is sputtered more or less, the output current in the forward

bias drops to lower values revealing the desired sputter fluence to be ~15 mC/cm^2. This is consistent with the other supplemental data, as the mid-sputtered region of the sample has a less disturbed Mo 3d core level as well as sharper LEED spots and displays the 2x2 reconstruction of the underlying N-terminated GaN.

Figure 5.10 displays the atomic force microscopy (AFM) images acquired for the outermost and inner sputter regions. Figure 5.10a corresponds to ~5 mC/cm^2, 5.10b to ~20 mC/cm^2, and 5.10c to ~35 mC/cm^2.

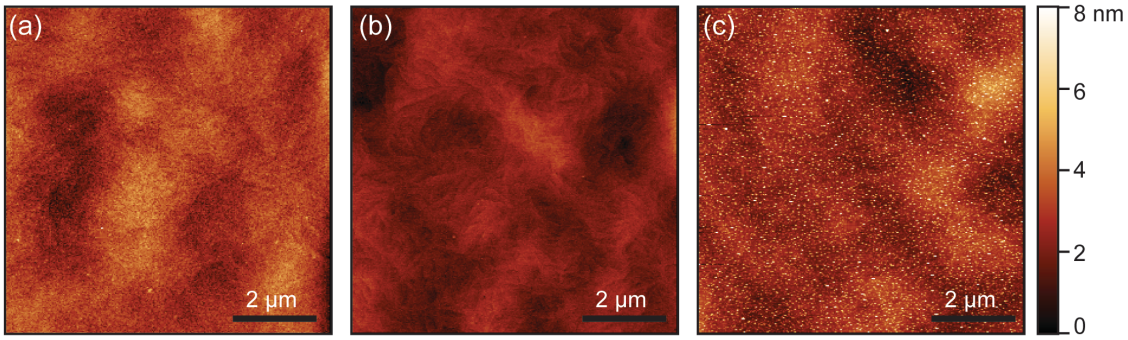

Figure 5.10 AFM topography maps of the (a) least sputtered, (b) mid-sputtered, and (c) most sputter areas of the substrate.

In figure 5.10c, the surface appears to be rougher and possible nucleation sites seemingly emerge from disordered growth atop the damaged GaN. This is also further confirmation that the Ne^+ sputter beam was too intense creating a rough and damaged GaN surface. MOCVD grown GaN typically exhibits some amount of terracing at the surface with clear steps. This can be seen in Figure 5.10a,b while the surface appears to be the cleanest and has the least height variation in the 20 mC/cm^2 region. This shows improved surface quality as an effect of the nitridation gradient, also reported by Zhang et. al.[115] They

report a cleaner surface after surface nitridation, clearly visible in figure 10a to figure 10b.

In conclusion, we were able to confirm a N-terminated gallium nitride by LEED measurements. We find that the best performing device, the less disturbed n-MoS_2 material, and the best surface topography is consistently in the ~15 mC/cm^2 region of the sample. This shows that through ion sputtering and NH_3 annealing, we are able to clean the surface of GaN successfully prior to MoS_2 deposition.

Summary

The high vacuum growth reactor has shown to systematically grow mono-, bi-, and trilayer MoS_2 material. This reactor is also not only able to grow MoS_2 material, but is extended to another TMD, NbS_2, showing versatility in this method. The high vacuum grown MoS_2 shows improved noise-transport characteristics as well as the possibility for integration with gold nanoparticles as a catalyst. The catalyst was shown to perform oxidation of carbon monoxide paving way for a cheaper alternative to other more costly materials. Due to the high vacuum environment, we may also tune the properties of heterostructures by an in-situ annealing treatment prior to MoS_2 deposition. This allows us to integrate cleanly by avoiding contamination between the two interfacing materials.

References

(1) Geim, A. K.; Novoselov, K. S. The Rise of Graphene. *Nat. Mater.* **2007**, *6*, 183.

(2) Manzeli, S.; Ovchinnikov, D.; Pasquier, D.; Yazyev, O. V.; Kis, A. 2D Transition Metal Dichalcogenides. *Nat. Rev. Mater.* **2017**, *2* (8), 17033. https://doi.org/10.1038/natrevmats.2017.33.

(3) Mak, K. F.; Lee, C.; Hone, J.; Shan, J.; Heinz, T. F. Atomically Thin MoS_2 : A New Direct-Gap Semiconductor. *Phys. Rev. Lett.* **2010**, *105* (13). https://doi.org/10.1103/PhysRevLett.105.136805.

(4) Splendiani, A.; Sun, L.; Zhang, Y.; Li, T.; Kim, J.; Chim, C.-Y.; Galli, G.; Wang, F. Emerging Photoluminescence in Monolayer MoS_2. *Nano Lett.* **2010**, *10* (4), 1271–1275. https://doi.org/10.1021/nl903868w.

(5) Suh, J.; Park, T.-E.; Lin, D.-Y.; Fu, D.; Park, J.; Jung, H. J.; Chen, Y.; Ko, C.; Jang, C.; Sun, Y.; Sinclair, R.; Chang, J.; Tongay, S.; Wu, J. Doping against the Native Propensity of MoS_2 : Degenerate Hole Doping by Cation Substitution. *Nano Lett.* **2014**, *14* (12), 6976–6982. https://doi.org/10.1021/nl503251h.

(6) Lu, C.-P.; Li, G.; Mao, J.; Wang, L.-M.; Andrei, E. Y. Bandgap, Mid-Gap States, and Gating Effects in MoS_2. *Nano Lett.* **2014**, *14* (8), 4628–4633. https://doi.org/10.1021/nl501659n.

(7) Smithe, K. K. H.; Suryavanshi, S. V.; Muñoz Rojo, M.; Tedjarati, A. D.; Pop, E. Low Variability in Synthetic Monolayer MoS_2 Devices. *ACS Nano* **2017**, *11* (8), 8456–8463. https://doi.org/10.1021/acsnano.7b04100.

(8) Kang, K.; Xie, S.; Huang, L.; Han, Y.; Huang, P. Y.; Mak, K. F.; Kim, C.-J.; Muller, D.; Park, J. High-Mobility Three-Atom-Thick Semiconducting Films with Wafer-Scale Homogeneity. *Nature* **2015**, *520* (7549), 656–660. https://doi.org/10.1038/nature14417.

(9) Pyeon, J. J.; Kim, S. H.; Jeong, D. S.; Baek, S.-H.; Kang, C.-Y.; Kim, J.-S.; Kim, S. K. Wafer-Scale Growth of MoS_2 Thin Films by Atomic Layer Deposition. *Nanoscale* **2016**, *8* (20), 10792–10798. https://doi.org/10.1039/C6NR01346E.

(10) Amano, H.; Sawaki, N.; Akasaki, I.; Toyoda, Y. Metalorganic Vapor Phase Epitaxial Growth of a High Quality GaN Film Using an AlN Buffer Layer. *Appl. Phys. Lett.* **1986**, *48* (5), 353–355. https://doi.org/10.1063/1.96549.

(11) Miwa, K.; Fukumoto, A. First-Principles Calculation of the Structural, Electronic, and Vibrational Properties of Gallium Nitride and Aluminum Nitride. *Phys. Rev. B* **1993**, *48* (11), 7897–7902. https://doi.org/10.1103/PhysRevB.48.7897.

(12) Sun, Q.; Cho, Y. S. Nitrogen-Polar GaN Growth Evolution on c-Plane Sapphire. *Appl Phys Lett* 4.

(13) Nakamura, S.; Mukai, T.; Senoh, M. High-Power GaN P-N Junction Blue-Light-Emitting Diodes. *Jpn. J. Appl. Phys.* **1991**, *30* (Part 2, No. 12A), L1998–L2001. https://doi.org/10.1143/JJAP.30.L1998.

(14) Amano, H.; Baines, Y.; Beam, E.; Borga, M.; Bouchet, T.; Chalker, P. R.; Charles, M.; Chen, K. J.; Chowdhury, N.; Chu, R.; De Santi, C.; De Souza, M. M.; Decoutere, S.; Di Cioccio, L.; Eckardt, B.; Egawa, T.; Fay, P.; Freedsman, J. J.; Guido, L.; Häberlen, O.; Haynes, G.; Heckel, T.; Hemakumara, D.; Houston, P.; Hu, J.; Hua, M.; Huang, Q.; Huang, A.; Jiang, S.; Kawai, H.; Kinzer, D.; Kuball, M.; Kumar, A.; Lee, K. B.; Li, X.; Marcon, D.; März, M.; McCarthy, R.; Meneghesso, G.; Meneghini, M.; Morvan, E.; Nakajima, A.; Narayanan, E. M. S.; Oliver, S.; Palacios, T.; Piedra, D.; Plissonnier, M.; Reddy, R.; Sun, M.; Thayne, I.; Torres, A.; Trivellin, N.; Unni, V.; Uren, M. J.; Van Hove, M.; Wallis, D. J.; Wang, J.; Xie, J.; Yagi, S.; Yang, S.; Youtsey, C.; Yu, R.; Zanoni, E.; Zeltner, S.; Zhang, Y. The 2018 GaN Power Electronics Roadmap. *J. Phys. Appl. Phys.* **2018**, *51* (16), 163001. https://doi.org/10.1088/1361-6463/aaaf9d.

(15) Lu, J.; Tian, Q.; Bai, K.; Brown, A.; McAmmond, M. An Indirect Matrix Converter Based 97%-Efficiency on-Board Level 2 Battery Charger Using E-Mode GaN HEMTs. In *2015 IEEE 3rd Workshop on Wide Bandgap Power Devices and Applications (WiPDA)*; IEEE: Blacksburg, VA, USA, 2015; pp 351–358. https://doi.org/10.1109/WiPDA.2015.7369258.

(16) Neugebauer, J.; Van de Walle, C. G. Atomic Geometry and Electronic Structure of Native Defects in GaN. *Phys. Rev. B* **1994**, *50* (11), 8067–8070. https://doi.org/10.1103/PhysRevB.50.8067.

(17) Sano, M.; Aoki, M. Epitaxial Growth of Undoped and Mg-Doped GaN. *Jpn. J. Appl. Phys.* **1976**, *15* (10), 1943–1950. https://doi.org/10.1143/JJAP.15.1943.

(18) Niwa, T.; Fujii, T.; Oka, T. High Carrier Activation of Mg Ion-Implanted GaN by Conventional Rapid Thermal Annealing. *Appl. Phys. Express* **2017**, *10* (9), 091002. https://doi.org/10.7567/APEX.10.091002.

(19) McDonnell, S.; Smyth, C.; Hinkle, C. L.; Wallace, R. M. MoS_2 –Titanium Contact Interface Reactions. *ACS Appl. Mater. Interfaces* **2016**, *8* (12), 8289–8294. https://doi.org/10.1021/acsami.6b00275.

(20) Zhou, D.; Shu, H.; Hu, C.; Jiang, L.; Liang, P.; Chen, X. Unveiling the Growth Mechanism of MoS_2 with Chemical Vapor Deposition: From Two-Dimensional Planar Nucleation to Self-Seeding Nucleation. *Cryst. Growth Des.* **2018**, *18* (2), 1012–1019. https://doi.org/10.1021/acs.cgd.7b01486.

(21) Zhu, D.; Shu, H.; Jiang, F.; Lv, D.; Asokan, V.; Omar, O.; Yuan, J.; Zhang, Z.; Jin, C. Capture the Growth Kinetics of CVD Growth of Two-Dimensional MoS_2. *Npj 2D Mater. Appl.* **2017**, *1* (1), 8. https://doi.org/10.1038/s41699-017-0010-x.

(22) Ji, Q.; Zhang, Y.; Zhang, Y.; Liu, Z. Chemical Vapour Deposition of Group-VIB Metal Dichalcogenide Monolayers: Engineered Substrates from Amorphous to Single Crystalline. *Chem. Soc. Rev.* **2015**, *44* (9), 2587–2602. https://doi.org/10.1039/C4CS00258J.

(23) Blake, P.; Hill, E. W.; Castro Neto, A. H.; Novoselov, K. S.; Jiang, D.; Yang, R.; Booth, T. J.; Geim, A. K. Making Graphene Visible. *Appl. Phys. Lett.* **2007**, *91* (6), 063124. https://doi.org/10.1063/1.2768624.

(24) Zhang, H.; Wan, Y.; Ma, Y.; Wang, W.; Wang, Y.; Dai, L. Interference Effect on Optical Signals of Monolayer MoS_2. *Appl. Phys. Lett.* **2015**, *107* (10), 101904. https://doi.org/10.1063/1.4930257.

(25) Plechinger, G.; Mann, J.; Preciado, E.; Barroso, D.; Nguyen, A.; Eroms, J.; Schüller, C.; Bartels, L.; Korn, T. A Direct Comparison of CVD-Grown and Exfoliated MoS_2 Using Optical Spectroscopy. *Semicond. Sci. Technol.* **2014**, *29* (6), 064008. https://doi.org/10.1088/0268-1242/29/6/064008.

(26) Johari, P.; Shenoy, V. B. Tunable Dielectric Properties of Transition Metal Dichalcogenides. *ACS Nano* **2011**, *5* (7), 5903–5908. https://doi.org/10.1021/nn201698t.

(27) Jiang, C.; Rumyantsev, S. L.; Samnakay, R.; Shur, M. S.; Balandin, A. A. High-Temperature Performance of MoS_2 Thin-Film Transistors: Direct Current and Pulse Current-Voltage Characteristics. *J. Appl. Phys.* **2015**, *117* (6), 064301. https://doi.org/10.1063/1.4906496.

(28) Singh, A. K.; Hwang, C.; Eom, J. Low-Voltage and High-Performance Multilayer MoS_2 Field-Effect Transistors with Graphene Electrodes. *ACS Appl. Mater. Interfaces* **2016**, *8* (50), 34699–34705. https://doi.org/10.1021/acsami.6b12217.

(29) Zhao, M.; Ye, Y.; Han, Y.; Xia, Y.; Zhu, H.; Wang, S.; Wang, Y.; Muller, D. A.; Zhang, X. Large-Scale Chemical Assembly of Atomically Thin Transistors and Circuits. *Nat. Nanotechnol.* **2016**, *11* (11), 954–959. https://doi.org/10.1038/nnano.2016.115.

(30) Baik, S. S.; Im, S.; Choi, H. J. Work Function Tuning in Two-Dimensional MoS_2 Field-Effect-Transistors with Graphene and Titanium Source-Drain Contacts. *Sci. Rep.* **2017**, *7* (1), 45546. https://doi.org/10.1038/srep45546.

(31) Andleeb, S.; Eom, J.; Rauf Naz, N.; Singh, A. K. MoS_2 Field-Effect Transistor with Graphene Contacts. *J. Mater. Chem. C* **2017**, *5* (32), 8308–8314. https://doi.org/10.1039/C7TC01736G.

(32) Radisavljevic, B.; Radenovic, A.; Brivio, J.; Giacometti, V.; Kis, A. Single-Layer MoS_2 Transistors. *Nat. Nanotechnol.* **2011**, *6* (3), 147–150. https://doi.org/10.1038/nnano.2010.279.

(33) Radisavljevic, B.; Kis, A. Reply to "Measurement of Mobility in Dual-Gated MoS_2 Transistors." *Nat. Nanotechnol.* **2013**, *8* (3), 147–148. https://doi.org/10.1038/nnano.2013.31.

(34) Fuhrer, M. S.; Hone, J. Measurement of Mobility in Dual-Gated MoS_2 Transistors. *Nat. Nanotechnol.* **2013**, *8* (3), 146–147. https://doi.org/10.1038/nnano.2013.30.

(35) Liu, H.; Ye, P. D. MoS_2 Dual-Gate MOSFET with Atomic-Layer-Deposited Al_2O_3 as Top-Gate Dielectric. 3.

(36) A. A. Balandin. *Noise and Fluctuations Control in Electronic Devices*; American Scientific Publishers: Stevenson Ranch, Calif., 2002.

(37) Balandin, A. A. Low-Frequency 1/f Noise in Graphene Devices. *Nat. Nanotechnol.* **2013**, *8* (8), 549–555. https://doi.org/10.1038/nnano.2013.144.

(38) Renteria, J.; Samnakay, R.; Rumyantsev, S. L.; Jiang, C.; Goli, P.; Shur, M. S.; Balandin, A. A. Low-Frequency 1/ *f* Noise in MoS_2 Transistors: Relative Contributions of the Channel and Contacts. *Appl. Phys. Lett.* **2014**, *104* (15), 153104. https://doi.org/10.1063/1.4871374.

(39) Rumyantsev, S. L.; Jiang, C.; Samnakay, R.; Shur, M. S.; Balandin, A. A. 1/ f Noise Characteristics of MoS_2 Thin-Film Transistors: Comparison of Single and Multilayer Structures. *IEEE Electron Device Lett.* **2015**, *36* (5), 517–519. https://doi.org/10.1109/LED.2015.2412536.

(40) Liu, G.; Rumyantsev, S.; Bloodgood, M. A.; Salguero, T. T.; Shur, M.; Balandin, A. A. Low-Frequency Electronic Noise in Quasi-1D $TaSe_3$ van Der Waals Nanowires. *Nano Lett.* **2017**, *17* (1), 377–383. https://doi.org/10.1021/acs.nanolett.6b04334.

(41) Dmitriev, A. P.; Levinshtein, M. E.; Rumyantsev, S. L. On the Hooge Relation in Semiconductors and Metals. *J. Appl. Phys.* **2009**, *106* (2), 024514. https://doi.org/10.1063/1.3186620.

(42) Rumyantsev, S.; Liu, G.; Stillman, W.; Shur, M.; Balandin, A. A. Electrical and Noise Characteristics of Graphene Field-Effect Transistors: Ambient Effects, Noise Sources and Physical Mechanisms. *J. Phys. Condens. Matter* **2010**, *22* (39), 395302. https://doi.org/10.1088/0953-8984/22/39/395302.

(43) Wang, J.-W.; Liu, Y.-P.; Chen, P.-H.; Chuang, M.-H.; Pezeshki, A.; Ling, D.-C.; Chen, J.-C.; Chen, Y.-F.; Lee, Y.-H. Controlled Low-Frequency Electrical Noise of Monolayer MoS_2 with Ohmic Contact and Tunable Carrier Concentration. *Adv. Electron. Mater.* **2018**, *4* (1), 1700340. https://doi.org/10.1002/aelm.201700340.

(44) Yang, J.; Mohmad, A. R.; Wang, Y.; Fullon, R.; Song, X.; Zhao, F.; Bozkurt, I.; Augustin, M.; Santos, E. J. G.; Shin, H. S.; Zhang, W.; Voiry, D.; Jeong, H. Y.; Chhowalla, M. Ultrahigh-Current-Density Niobium Disulfide Catalysts for Hydrogen Evolution. *Nat. Mater.* **2019**, *18* (12), 1309–1314. https://doi.org/10.1038/s41563-019-0463-8.

(45) Bark, H.; Choi, Y.; Jung, J.; Kim, J. H.; Kwon, H.; Lee, J.; Lee, Z.; Cho, J. H.; Lee, C. Large-Area Niobium Disulfide Thin Films as Transparent Electrodes for Devices Based on Two-Dimensional Materials. *Nanoscale* **2018**, *10* (3), 1056–1062. https://doi.org/10.1039/C7NR07593F.

(46) Kim, Y.; Kwon, K. C.; Kang, S.; Kim, C.; Kim, T. H.; Hong, S.-P.; Park, S. Y.; Suh, J. M.; Choi, M.-J.; Han, S.; Jang, H. W. Two-Dimensional NbS_2 Gas Sensors for Selective and Reversible NO_2 Detection at Room Temperature. *ACS Sens.* **2019**, *4* (9), 2395–2402. https://doi.org/10.1021/acssensors.9b00992.

(47) Li, Z.; Yang, W.; Losovyj, Y.; Chen, J.; Xu, E.; Liu, H.; Werbianskyj, M.; Fertig, H. A.; Ye, X.; Zhang, S. Large-Size Niobium Disulfide Nanoflakes down to Bilayers Grown by Sulfurization. *Nano Res.* **2018**, *11* (11), 5978–5988. https://doi.org/10.1007/s12274-018-2111-z.

(48) Haruta, M.; Kobayashi, T.; Sano, H.; Yamada, N. Novel Gold Catalysts for the Oxidation of Carbon Monoxide at a Temperature Far Below 0 °C. *Chem. Lett.* **1987**, *16* (2), 405–408. https://doi.org/10.1246/cl.1987.405.

(49) Hammer, B.; Norskov, J. K. Why Gold Is the Noblest of All the Metals. *Nature* **1995**, *376* (6537), 238–240. https://doi.org/10.1038/376238a0.

(50) Haruta, M.; Tsubota, S.; Kobayashi, T.; Kageyama, H.; Genet, M. J.; Delmon, B. Low-Temperature Oxidation of CO over Gold Supported on TiO_2, α-Fe_2O_3, and Co3O4. *J. Catal.* **1993**, *144* (1), 175–192. https://doi.org/10.1006/jcat.1993.1322.

(51) Schubert, M. M.; Plzak, V.; Garche, J.; Behm, R. J. Activity, Selectivity, and Long-Term Stability of Different Metal Oxide Supported Gold Catalysts for the Preferential CO Oxidation in H_2-Rich Gas. *Catal. Lett.* **2001**, *76* (3), 143–150. https://doi.org/10.1023/A:1012365710979.

(52) Deng, W.; Jesus, J. D.; Saltsburg, H.; Flytzani-Stephanopoulos, M. Low-Content Gold-Ceria Catalysts for the Water–Gas Shift and Preferential CO Oxidation Reactions. *Appl. Catal. Gen.* **2005**, *291* (1–2), 126–135. https://doi.org/10.1016/j.apcata.2005.02.048.

(53) Gardner, S. D.; Hoflund, G. B.; Schryer, D. R.; Schryer, Jacqueline.; Upchurch, B. T.; Kielin, E. J. Catalytic Behavior of Noble Metal/Reducible Oxide Materials for Low-Temperature Carbon Monoxide Oxidation. 1. Comparison of Catalyst Performance. *Langmuir* **1991**, *7* (10), 2135–2139. https://doi.org/10.1021/la00058a027.

(54) Chen, M. S.; Goodman, D. W. The Structure of Catalytically Active Gold on Titania. *Science* **2004**, *306* (5694), 252. https://doi.org/10.1126/science.1102420.

(55) Zhou, Y. Y. Resonant Photoemission Observations and DFT Study of S-d-Hybridization in Catalytically Active Gold Clusters on Ceria Nanorods. *Angew Chem Int Ed* **2013**, *52*, 6936.

(56) Yang, F.; Graciani, J.; Evans, J.; Liu, P.; Hrbek, J.; Sanz, J. F.; Rodriguez, J. A. CO Oxidation on Inverse CeO_x/Cu(111) Catalysts: High Catalytic Activity and Ceria-Promoted Dissociation of O_2. *J Am Chem Soc* **2011**, *133*, 3444.

(57) Merida, C. S. Gold Dispersion and Activation on the Basal Plane of Single-Layer MoS_2. *J Phys Chem C* **2018**, *122*, 267.

(58) Wang, B.; Bocquet, M. L. Monolayer Graphene and H-BN on Metal Substrates as Versatile Templates for Metallic Nanoclusters. *J Phys Chem Lett* **2011**, *2*, 2341.

(59) Rawal, T. B.; Le, D.; Rahman, T. S. Effect of Single-Layer MoS2 on the Geometry, Electronic Structure, and Reactivity of Transition Metal Nanoparticles. *J Phys Chem C* **2017**, *121*, 7282.

(60) Katsiev, K.; Losovyj, Y.; Lozova, N.; Wang, L.; Mei, W. N.; Zheng, J. X.; Vescovo, E.; Liu, L.; Dowben, P. A.; Goodman, D. W. The Band Structure of Carbonmonoxide on 2-D Au Islands on Graphene. *Appl Surf Sci* **2014**, *304*, 35.

(61) Zheng, J. X.; Wang, L.; Katsiev, K.; Losovyj, Y.; Vescovo, E.; Goodman, D. W.; Dowben, P. A.; Lu, J.; Mei, W. N. Adsorption Configurations of Carbon Monoxide on Gold Monolayer Supported by Graphene or Monolayer Hexagonal Boron Nitride: A First-Principles Study. *Eur Phys J B* **2013**, *86*, 441.

(62) Hansen, L. P.; Ramasse, Q. M.; Kisielowski, C.; Brorson, M.; Johnson, E.; Topsoe, H.; Helveg, S. Atomic-Scale Edge Structures on Industrial-Style MoS_2 Nanocatalysts. *Angew Chem Int Ed* **2011**, *50*, 10153.

(63) Surisetty, V. R.; Dalai, A. K.; Kozinski, J. Alcohols as Alternative Fuels: An Overview. *Appl Catal A* **2011**, *404*, 1.

(64) Saito, M.; Anderson, R. B. The Activity of Molybdenum Compounds for the Methanation of CO2. *J Catal* **1981**, *67*, 296.

(65) Osaki, T.; Narita, N.; Horiuchi, T.; Sugiyama, T.; Masuda, H.; Suzuki, K. Kinetics of Reverse Water Gas Shift (RWGS) Reaction on Metal Disulfide Catalysts. *J Mol Catal Chem* **1997**, *125*, 63.

(66) Kim, J.; Byun, S.; Smith, A. J.; Yu, J.; Huang, J. X. Enhanced Electrocatalytic Properties of Transition-Metal Dichalcogenides Sheets by Spontaneous Gold Nanoparticle Decoration. *J Phys Chem Lett* **2013**, *4*, 1227.

(67) Besenbacher, F.; Brorson, M.; Clausen, B. S.; Helveg, S.; Hinnemann, B.; Kibsgaard, J.; Lauritsen, J.; Moses, P. G.; Norskov, J. K.; Topsoe, H. Recent STM, DFT and HAADF-STEM Studies of Sulfide-Based Hydrotreating Catalysts: Insight into Mechanistic, Structural and Particle Size Effects. *Catal Today* **2008**, *130*, 86.

(68) Sun, D.; Lu, W.; Le, D.; Ma, Q.; Aminpour, M.; Alcántara Ortigoza, M.; Bobek, S.; Mann, J.; Wyrick, J.; Rahman, T. S.; Bartels, L. An MoSx Structure with High Affinity for Adsorbate Interaction. *Angew Chem* **2012**, *124*, 10430.

(69) Kibsgaard, J.; Chen, Z. B.; Reinecke, B. N.; Jaramillo, T. F. Engineering the Surface Structure of MoS_2 to Preferentially Expose Active Edge Sites for Electrocatalysis. *Nat Mater* **2012**, *11*, 963.

(70) Ho, T. A.; Bae, C.; Lee, S.; Kim, M.; Montero-Moreno, J. M.; Park, J. H.; Shin, H. Edge-on MoS_2 Thin Films by Atomic Layer Deposition for Understanding the Interplay between the Active Area and Hydrogen Evolution Reaction. *Chem Mater* **2017**, *29*, 7604.

(71) Ma, Q. Controlled Argon Beam-Induced Desulfurization of Monolayer Molybdenum Disulfide. *J Phys Condens Matter* **2013**, *25*, 252201.

(72) Ma, Q. Postgrowth Tuning of the Bandgap of Single-Layer Molybdenum Disulfide Films by Sulfur/Selenium Exchange. *ACS Nano* **2014**, *8*, 4672.

(73) Le, D.; Rawal, T. B.; Rahman, T. S. Single-Layer MoS_2 with Sulfur Vacancies: Structure and Catalytic Application. *J Phys Chem C* **2014**, *118*, 5346.

(74) Le, D.; Rahman, T. S. Joined Edges in Mos2: Metallic and Half-Metallic Wires. *J Phys Condens Matter* **2013**, *25*, 312201.

(75) Valden, M.; Lai, X.; Goodman, D. W. Onset of Catalytic Activity of Gold Clusters on Titania with the Appearance of Nonmetallic Properties. *Science* **1998**, *281*, 1647.

(76) Lopez, N.; Janssens, T. V. W.; Clausen, B. S.; Xu, Y.; Mavrikakis, M.; Bligaard, T.; Norskov, J. K. On the Origin of the Catalytic Activity of Gold Nanoparticles for Low-Temperature CO Oxidation. *J Catal* **2004**, *223*, 232.

(77) Bondzie, V. A.; Parker, S. C.; Campbell, C. T. The Kinetics of Co Oxidation by Adsorbed Oxygen on Well-Defined Gold Particles on TiO_2(110). *Catal Lett* **1999**, *63*, 143.

(78) McKee, W. C.; Patterson, M. C.; Huang, D.; Frick, J. R.; Kurtz, R. L.; Sprunger, P. T.; Liu, L.; Xu, Y. CO Adsorption on Au Nanoparticles Grown on Hexagonal Boron Nitride/Rh(111). *J Phys Chem C* **2016**, *120*, 10909.

(79) Ng, M. L.; Preobrajenski, A. B.; Vinogradov, A. S.; Martensson, N. Formation and Temperature Evolution of Au Nanoparticles Supported on the H-BN Nanomesh. *Surf Sci* **2008**, *602*, 1250.

(80) Niraula, I. B.; Kengne, B. A. F.; McIlroy, D. N. Gas Phase Interactions at the Surface of Bare and Gold Nanoparticle Decorated Gallium Nitride Nanowires by Ultraviolet Photoelectron Spectroscopy. *Phys Rev B Condens Matter Mater Phys* **2012**, *86*, 155437.

(81) Almeida, K.; Wurch, M.; Geremew, A.; Yamaguchi, K.; Empante, T. A.; Valentin, M. D.; Gomez, M.; Berges, A. J.; Stecklein, G.; Rumyantsev, S.; Martinez, J.; Balandin, A. A.; Bartels, L. High-Vacuum Particulate-Free Deposition of Wafer-Scale Mono-, Bi-, and Trilayer Molybdenum Disulfide with Superior Transport Properties. *ACS Appl. Mater. Interfaces* **2018**, *10* (39), 33457–33463. https://doi.org/10.1021/acsami.8b10857.

(82) Lee, C.; Yan, H.; Brus, L. E.; Heinz, T. F.; Hone, J.; Ryu, S. Anomalous Lattice Vibrations of Single- and Few-Layer MoS_2. *ACS Nano* **2010**, *4*, 2695.

(83) Tahersima, M. H. Testbeds for Transition Metal Dichalcogenide Photonics: Efficacy of Light Emission Enhancement in Monomer Vs Dimer Nanoscale Antennae. *ACS Photonics* **2017**, *4*, 1713.

(84) Kresse, G.; Furthmuller, J. Efficiency of Ab-Initio Total Energy Calculations for Metals and Semiconductors Using a Plane-Wave Basis Set. *Comput Mater Sci* **1996**, *6*, 15.

(85) Blöchl, P. E. Projector Augmented-Wave Method. *Phys Rev B Condens Matter Mater Phys* **1994**, *50*, 17953.

(86) Kresse, G.; Joubert, D. From Ultrasoft Pseudopotentials to the Projector Augmented-Wave Method. *Phys Rev B Condens Matter Mater Phys* **1999**, *59*, 1758.

(87) Klimeš, J.; Bowler, D. R.; Michaelides, A. Van Der Waals Density Functionals Applied to Solids. *Phys Rev B Condens Matter Mater Phys* **2011**, *83*, 195131.

(88) Klimeš, J.; Bowler, D. R.; Michaelides, A. Chemical Accuracy for the van Der Waals Density Functional. *J Phys Condens Matter* **2010**, *22*, 022201.

(89) Mittendorfer, F.; Garhofer, A.; Redinger, J.; Klimes, J.; Harl, J.; Kresse, G. Graphene on Ni(111): Strong Interaction and Weak Adsorption. *Phys Rev B Condens Matter Mater Phys* **2011**, *84*, 201401R.

(90) Okazaki, K.; Ichikawa, S.; Maeda, Y.; Haruta, M.; Kohyama, M. Electronic Structures of Au Supported on TiO_2. *Appl Catal A* **2005**, *291*, 45.

(91) Liu, P.; Rodriguez, J. A. Water-Gas-Shift Reaction on Metal Nanoparticles and Surfaces. *J Chem Phys* **2007**, *126*, 164705.

(92) Henkelman, G.; Uberuaga, B. P.; Jonsson, H. A Climbing Image Nudged Elastic Band Method for Finding Saddle Points and Minimum Energy Paths. *J Chem Phys* **2000**, *113*, 9901.

(93) Yue, Q.; Shao, Z. Z.; Chang, S. L.; Li, J. B. Adsorption of Gas Molecules on Monolayer MoS_2 and Effect of Applied Electric Field. *Nanoscale Res Lett* **2013**, *8*, 425.

(94) Mehmood, F.; Kara, A.; Rahman, T. S.; Henry, C. R. Comparative Study of CO Adsorption on Flat, Stepped, and Kinked Au Surfaces Using Density Functional Theory. *Phys Rev B Condens Matter Mater Phys* **2009**, *79*, 075422.

(95) Grim, R. G. [National R. E. Lab. (NREL), Golden, CO (United States)]; To, A. T. [National R. E. Lab. (NREL), Golden, CO (United States)]; Farberow, C. A. [National R. E. Lab. (NREL), Golden, CO (United States)]; Hensley, J. E. [National R. E. Lab. (NREL), Golden, CO (United States)]; Ruddy, D. A. [National R. E. Lab. (NREL), Golden, CO (United States)]; Schaidle, J. A. [National R. E. Lab. (NREL), Golden, CO (United States)]. Growing the Bioeconomy through Catalysis: A Review of Recent Advancements in the Production of Fuels and Chemicals from Syngas-Derived Oxygenates. *ACS Catal.* **2019**. https://doi.org/10.1021/acscatal.8b03945.

(96) Bai, H.; Ma, M.; Bai, B.; Cao, H.; Zhang, L.; Gao, Z.; Vinokurov, V. A.; Huang, W. Carbon Chain Growth by Formyl Coupling over the Cu/γ-AlOOH(001) Surface in Syngas Conversion. *Phys. Chem. Chem. Phys.* **2019**, *21* (1), 148–159. https://doi.org/10.1039/C8CP06582A.

(97) Choi, Y.; Liu, P. Mechanism of Ethanol Synthesis from Syngas on Rh(111). *J. Am. Chem. Soc.* **2009**, *131* (36), 13054–13061. https://doi.org/10.1021/ja903013x.

(98) Almeida, K.; Peña, P.; Rawal, T. B.; Coley, W. C.; Akhavi, A.-A.; Wurch, M.; Yamaguchi, K.; Le, D.; Rahman, T. S.; Bartels, L. A Single Layer of MoS_2 Activates Gold for Room Temperature CO Oxidation on an Inert Silica Substrate. *J. Phys. Chem. C* **2019**, *123* (11), 6592–6598. https://doi.org/10.1021/acs.jpcc.8b12325.

(99) Morrill, M. R.; Thao, N. T.; Shou, H.; Davis, R. J.; Barton, D. G.; Ferrari, D.; Agrawal, P. K.; Jones, C. W. Origins of Unusual Alcohol Selectivities over Mixed MgAl Oxide-Supported K/MoS_2 Catalysts for Higher Alcohol Synthesis from Syngas. *ACS Catal.* **2013**, *3* (7), 1665–1675. https://doi.org/10.1021/cs400147d.

(100) Taborga Claure, M.; Chai, S.-H.; Dai, S.; Unocic, K. A.; Alamgir, F. M.; Agrawal, P. K.; Jones, C. W. Tuning of Higher Alcohol Selectivity and Productivity in CO Hydrogenation Reactions over K/MoS_2 Domains Supported on Mesoporous Activated Carbon and Mixed MgAl Oxide. *J. Catal.* **2015**, *324*, 88–97. https://doi.org/10.1016/j.jcat.2015.01.015.

(101) Surisetty, V. R.; Dalai, A. K.; Kozinski, J. Synthesis of Higher Alcohols from Synthesis Gas over Co-Promoted Alkali-Modified MoS_2 Catalysts Supported on MWCNTs. *Appl. Catal. Gen.* **2010**, *385* (1), 153–162. https://doi.org/10.1016/j.apcata.2010.07.009.

(102) Lv, M.; Xie, W.; Sun, S.; Wu, G.; Zheng, L.; Chu, S.; Gao, C.; Bao, J. Activated-Carbon-Supported K–Co–Mo Catalysts for Synthesis of Higher Alcohols from Syngas. *Catal. Sci. Technol.* **2015**, *5* (5), 2925–2934. https://doi.org/10.1039/C5CY00083A.

(103) Xie, W.; Zhou, J.; Ji, L.; Sun, S.; Pan, H.; Zhu, J.; Gao, C.; Bao, J. Targeted Design and Synthesis of a Highly Selective Mo-Based Catalyst for the Synthesis of Higher Alcohols. *RSC Adv.* **2016**, *6* (45), 38741–38745. https://doi.org/10.1039/C6RA05332G.

(104) Luk, H. T.; Mondelli, C.; Ferré, D. C.; Stewart, J. A.; Pérez-Ramírez, J. Status and Prospects in Higher Alcohols Synthesis from Syngas. *Chem. Soc. Rev.* **2017**, *46* (5), 1358–1426. https://doi.org/10.1039/C6CS00324A.

(105) Luk, H. T.; Forster, T.; Mondelli, C.; Siol, S.; Curulla-Ferré, D.; Stewart, J. A.; Pérez-Ramírez, J. Carbon Nanofibres-Supported KCoMo Catalysts for Syngas Conversion into Higher Alcohols. *Catal. Sci. Technol.* **2018**, *8* (1), 187–200. https://doi.org/10.1039/C7CY01908D.

(106) Ao, M.; Pham, G. H.; Sunarso, J.; Tade, M. O.; Liu, S. Active Centers of Catalysts for Higher Alcohol Synthesis from Syngas: A Review. *ACS Catal.* **2018**, *8* (8), 7025–7050. https://doi.org/10.1021/acscatal.8b01391.

(107) Rawal, T. B.; Le, D.; Rahman, T. S. MoS_2-Supported Gold Nanoparticle for CO Hydrogenation. *J. Phys. Condens. Matter* **2017**, *29* (41), 415201. https://doi.org/10.1088/1361-648x/aa8314.

(108) Perdew, J. P.; Burke, K.; Ernzerhof, M. Generalized Gradient Approximation Made Simple. *Phys. Rev. Lett.* **1996**, *77* (18), 3865–3868. https://doi.org/10.1103/PhysRevLett.77.3865.

(109) Grimme, S.; Antony, J.; Ehrlich, S.; Krieg, H. A Consistent and Accurate *Ab Initio* Parametrization of Density Functional Dispersion Correction (DFT-D) for the 94 Elements H-Pu. *J. Chem. Phys.* **2010**, *132* (15), 154104. https://doi.org/10.1063/1.3382344.

(110) Prins, R.; Egorova, M.; Röthlisberger, A.; Zhao, Y.; Sivasankar, N.; Kukula, P. Mechanisms of Hydrodesulfurization and Hydrodenitrogenation. *Front. Catal. Mol. View Ind. Catal.* **2006**, *111* (1), 84–93. https://doi.org/10.1016/j.cattod.2005.10.008.

(111) Gupta, P.; Rahman, A. A.; Subramanian, S.; Gupta, S.; Thamizhavel, A.; Orlova, T.; Rouvimov, S.; Vishwanath, S.; Protasenko, V.; Laskar, M. R.; Xing, H. G.; Jena, D.; Bhattacharya, A. Layered Transition Metal Dichalcogenides: Promising near-Lattice-Matched Substrates for GaN Growth. *Sci. Rep.* **2016**, *6* (1), 23708. https://doi.org/10.1038/srep23708.

(112) Moun, M.; Kumar, M.; Garg, M.; Pathak, R.; Singh, R. Understanding of MoS_2/GaN Heterojunction Diode and Its Photodetection Properties. *Sci. Rep.* **2018**, *8* (1), 11799. https://doi.org/10.1038/s41598-018-30237-8.

(113) Ruzmetov, D.; Neupane, M. R.; Herzing, A.; O'Regan, T. P.; Mazzoni, A.; Chin, M. L.; Burke, R. A.; Crowne, F. J.; Glen Birdwell, A.; Taylor, D. E.; Kolmakov, A.;

Zhang, K.; Robinson, J. A.; Davydov, A. V.; Ivanov, T. G. Van Der Waals Interfaces in Epitaxial Vertical Metal/2D/3D Semiconductor Heterojunctions of Monolayer MoS_2 and GaN. *2D Mater.* **2018**, *5* (4), 045016. https://doi.org/10.1088/2053-1583/aad1b7.

(114) Lai, Y.-H.; Yeh, C.-T.; Hwang, J.-M.; Hwang, H.-L.; Chen, C.-T.; Hung, W.-H. Sputtering and Etching of GaN Surfaces. *J. Phys. Chem. B* **2001**, *105* (41), 10029–10036. https://doi.org/10.1021/jp011728k.

(115) Zhang, Z.; Li, B.; Qian, Q.; Tang, X.; Hua, M.; Huang, B.; Chen, K. J. Revealing the Nitridation Effects on GaN Surface by First-Principles Calculation and X-Ray/Ultraviolet Photoemission Spectroscopy. *IEEE Trans. Electron Devices* **2017**, *64* (10), 4036–4043. https://doi.org/10.1109/TED.2017.2733547.

(116) Liu, D.; Guo, Y.; Fang, L.; Robertson, J. Sulfur Vacancies in Monolayer MoS_2 and Its Electrical Contacts. *Appl Phys Lett* **2014**, 5.

(117) Greco, G.; Iucolano, F.; Roccaforte, F. Ohmic Contacts to Gallium Nitride Materials. *Appl. Surf. Sci.* **2016**, *383*, 324–345. https://doi.org/10.1016/j.apsusc.2016.04.016.